Received: 5 May 2025 | Revised: 28 October 2025 | Accepted: 31 October 2025

DOI: 10.1111/bph.70277

RESEARCH ARTICLE

Molecular glue neferine induces BAP31 homodimerisation to disrupt endoplasmic reticulum–mitochondria crosstalk for anti-neuroinflammation in ischaemic stroke

Ya-Xuan Zhu[1] | Zhuo Yang[1] | Ling Li[1] | Ze-Kun Chen[1,2] | Fang-Fang Zhuo[1] | Yu-Hui Wang[3] | Zheng-Ping Liu[4] | Bo Han[5] | Wei Yu[5] | Peng-Fei Tu[1] | Tian-Tian Wei[1] | Hua Wang[6,7] | Ke-Wu Zeng[1,2]

[1]State Key Laboratory of Natural and Biomimetic Drugs, School of Pharmaceutical Sciences, Peking University, Beijing, China

[2]Department of Integration of Chinese and Western Medicine, School of Basic Medical Sciences, Peking University, Beijing, China

[3]The Research Center of Chiral Drugs, Innovation Research Institute of Traditional Chinese Medicine, Shanghai University of Traditional Chinese Medicine, Shanghai, China

[4]Shandong Academy of Pharmaceutical Sciences, New Sustained and Controlled Release Formulations and Drug Targeted Delivery System Shandong Engineering Research Center, Jinan, China

[5]School of Pharmacy/Key Laboratory of Xinjiang Phytomedicine Resource and Utilization, Shihezi University, Shihezi, China

[6]Department of Oncology, The First Affiliated Hospital of Anhui Medical University, Hefei, China

[7]Key Laboratory of Anti-inflammatory and Immune Medicine (Anhui Medical University), Ministry of Education, Hefei, China

Correspondence

Tian-Tian Wei and Ke-Wu Zeng, State Key Laboratory of Natural and Biomimetic Drugs, School of Pharmaceutical Sciences, Peking University, Beijing 100191, China.
Email: wtt@bjmu.edu.cn;
Email: zkw@bjmu.edu.cn

Hua Wang, Department of Oncology, The First Affiliated Hospital of Anhui Medical University, Hefei, 230022, China.
Email: wanghua@ahmu.edu.cn

Funding information

Jinan New 20 Policies for Higher Education Funding, Grant/Award Number: 202228048; National Natural Sciences Foundation of

Background and Purpose: B-cell receptor-associated protein 31 (BAP31), an endoplasmic reticulum (ER)-resident transmembrane protein, has emerged as a critical regulator of immune cell activation, yet its role in neuroinflammation remains unexplored. Here, we uncovered the natural compound neferine (Nef) as a pharmacological modulator of BAP31 that suppressed microglial activation.

Experimental Approach: Using thermal protein profiling (TPP), we identified BAP31 as the primary target of Nef. Biochemical and structural analyses were employed to characterise Nef-BAP31 interactions. We evaluated ER stress and mitochondrial energy metabolism homeostasis using techniques such as STER super-resolution technology, flow cytometry, western blot, *etc*. In vivo validation utilised two models: lipopolysaccharide (LPS)-induced endotoxaemia and middle cerebral artery occlusion (MCAO) for ischaemic stroke, combining behavioural tests, cytokine profiling and histopathological assessments.

Key Results: Nef functioned as a ‘molecular glue’ by binding to BAP31's coiled-coil CC2 domain to induce stable dimerisation. We revealed that dimerised BAP31 triggered ER membrane remodelling, which disrupted ER–mitochondria contact sites and preserved mitochondrial energy metabolism homeostasis, thereby blocking inflammatory cytokine release. In vivo, Nef attenuated neuroinflammation in endotoxaemia mice and further conferred neuroprotection against ischaemic stroke in a MCAO model by inhibiting microglia-driven neuronal injury.

Conclusions and Implications: In summary, our work reveals that BAP31 is a master regulator of ER-mitochondria communication during microglial activation and introduces a paradigm-shifting ‘molecular glue’ strategy for targeting ER-resident proteins. Additionally, these findings redefine the pharmacological landscape for modulating organelle interactions in microglia involved in neuroinflammatory diseases.

Abbreviations: Arm, armepavine; BAP31, B cell receptor-associated protein 31; CHOP, C/EBP-homologous protein; HSP60, heat shock protein 60; iNOS, inducible nitric oxide synthase; IRE1α, inositol-requiring enzyme type 1 α; Nef, neferine; PERK, protein kinase RNA-like endoplasmic reticulum kinase.

China, Grant/Award Numbers: 82174008, 82325050, U23A20529; Beijing Municipal Natural Science Foundation-Key Research Project of the Daxing, Grant/Award Number: L246029; Beijing Municipal Natural Science Foundation, Grant/Award Number: 7232273; Natural Science Foundation of Shandong Province (Joint Foundation for Innovation and Development), Grant/Award Number: ZR2022LZY021; Special Fund for “Tian-Chi Talent Introduction Program”; Special Fund for Taishan Scholars Project in Shandong Province, Grant/Award Number: tstp20230633

KEYWORDS

B cell receptor-associated protein 31 (BAP31), endoplasmic reticulum (ER), ischaemic stroke, microglial polarization, neferine (Nef), neuroinflammation

1 | INTRODUCTION

B-cell receptor-associated protein 31 (BAP31) is a 28 kDa protein that belongs to the B-cell receptor-associated protein (BAP) family (Kim et al., 1994). BAP31 is widely expressed in the endoplasmic reticulum (ER) membrane and is classified as a resident protein of the ER. BAP31 also has been implicated in diverse biological processes, including protein transport (Annaert et al., 1997; Zen et al., 2004), apoptosis (Ng et al., 1997) and immune activation (Niu et al., 2017). Recent studies have demonstrated that BAP31 is significantly overexpressed in immune cells and plays a crucial role in immune cell proliferation and activation (B. Zhao et al., 2024), as well as immunogenic cell death (Panaretakis et al., 2009). Particularly, BAP31 plays a significant role in the activation of microglia and neuroinflammation, contributing to the progression of various central nervous system disorders, including Alzheimer's disease (AD), Parkinson's disease (PD) and amyotrophic lateral sclerosis (ALS) (Kuijpers et al., 2013; Liu et al., 2019; Wang et al., 2019). Therefore, it is speculated that targeting BAP31 represents a promising approach to safeguarding the nervous system by suppressing the onset of inflammatory responses. However, there are currently no reported neuroprotective drugs that specifically target BAP31.

BAP31, a member of the BAP family, possesses evolutionarily conserved sequence characteristics (Kim et al., 1994). BAP31 consists of three transmembrane helices (TM1, TM2 and TM3) and two coiled-coil structures (CC1 and CC2) (Quistgaard et al., 2013). Therefore, BAP31 can self-assemble into homodimers through domain interactions, which subsequently aggregate to form oligomers that regulate various cellular functions (Abe et al., 2009; Breckenridge et al., 2002; Ng et al., 1997; Nguyen et al., 2000; Quistgaard et al., 2013). Moreover, BAP31 is predominantly cleaved by **caspase-8** at the distal cleavage site. This process results in the conversion of the full-length 28-kDa BAP31 (p28-BAP31) into a 20-kDa fragment as p20-BAP31 (Ng et al., 1997). In particular, recent studies have demonstrated that p20-BAP31 induces calcium release from the ER, subsequently facilitating rapid uptake by adjacent mitochondria for crosstalk (Breckenridge et al., 2003; Heath-Engel et al., 2012).

The interaction between the ER and mitochondria is vital for cellular immune regulation. Mitochondria-associated membranes (MAMs) are specialised membrane domains within the ER that are associated with mitochondria (Marchi et al., 2014). In fact, the MAMs of the ER can interact with the outer mitochondrial membrane via protein–protein interactions (Hayashi & Su, 2007; Rizzuto et al., 1993; Szabadkai et al., 2006). Moreover, previous studies have demonstrated that BAP31 is extensively distributed in MAMs and plays a crucial role in promoting crosstalk between the ER and mitochondria through the proteins Fis1 and TOM40 (Iwasawa et al., 2011; T. Namba, 2019). Notably, the interaction between the ER and mitochondria mediated by BAP31 is essential for maintaining cellular energy homeostasis by protecting the mitochondrial membrane (Chandra et al., 2004; Cho et al., 2017; Myhill et al., 2008; T. Namba et al., 2013). Moreover, the ER–mitochondria interaction regulates several inflammatory signalling pathways, including NF-κB, MAPK and **IRAK1**, and plays a critical role in the immune response (Hendrickx

What is already known?

- No specific neuroprotective drugs targeting BAP31 have been reported.
- BAP31 regulates ER–mitochondria contact sites for microglial activation.

What does this study add?

- Neferine directly induces the BAP31 homodimerisation to inhibit microglia.
- Neferine disrupts ER–mitochondria crosstalk via BAP31–HSP60 interaction.

What is the clinical significance?

- Neferine is a lead drug molecule for the treatment of ischaemic stroke.
- Targeting ER–mitochondria crosstalk is a strategy against neuroinflammation.

et al., 2003; Rao et al., 2014; Yamazaki et al., 2009). However, there are currently no reports indicating that BAP31 functions as a druggable target in the interaction between the ER and mitochondria, an interaction that has significant implications for the inhibition of immune activation and inflammatory diseases.

In this study, we systematically characterised the natural alkaloid **neferine** (Nef) as a pharmacological agent that suppressed microglial activation by targeting BAP31. Through thermal protein profiling (TPP), we identified BAP31 as the primary cellular target of Nef. Crucially, Nef bound to the coiled-coil CC2 domain of BAP31, acting as a ‘molecular glue’ to induce its functional dimerisation. This dimerisation disrupted the BAP31-**HSP60** complex at ER–mitochondria contact sites. Consequently, Nef effectively preserved mitochondrial energy homeostasis by enhancing **ATP** synthesis and reducing reactive oxygen species accumulation, thereby suppressing the mitochondrial-related TNF-α signalling pathway in activated microglia. In vivo, Nef attenuated neuroinflammation in endotoxaemia mice and rescued neuronal apoptosis in a middle cerebral artery occlusion (MCAO) model, demonstrating therapeutic efficacy against ischaemic stroke.

In summary, this study addresses critical gaps in organelle pharmacology by demonstrating the role of the ER–mitochondria interaction in regulating microglial polarisation responses. Furthermore, our findings enhance the mechanistic understanding of BAP31, and these findings have implications for the development of future anti-neuroinflammatory drugs.

2 | METHODS

2.1 | Materials

Neferine (Nef, $C_{38}H_{44}N_2O_6$) and armepavine (Arm, $C_{19}H_{23}NO_3$) were obtained from Must (Chengdu) BioTechnology (Chengdu, China) with a purity greater than 98% by HPLC. Dulbecco's modified Eagle's medium (DMEM) was purchased from Gibco (Billings, MT, USA). Fetal bovine serum (FBS) was purchased from ABW (Shanghai, China). MTT was from Sigma-Aldrich Chemical (Saint Louis, MO, USA). Nitric oxide detection kits were purchased from Jiancheng (Nanjing, Jiangsu, China) The cell painting dyes, MitoTracker, Lipofectamine RNAiMAX and Lipofectamine 2000 were obtained from Invitrogen (Thermo Fisher Scientific, Waltham, MA, USA). The Opti-MEM was from Gibco (Thermo Fisher Scientific, Waltham, MA, USA). The MolPure Cell/Tissue Total RNA Kit, Hifair III First Strand cDNA Synthesis SuperMix and Hieff qPCR SYBR Green Master Mix were purchased from YEASEN (Shanghai, China). Primary antibody for mouse anti-β-actin (1:1000, Abcam Cat# ab8226, RRID: AB_306371), mouse anti-BAP31 (1:1000, Abcam Cat# ab112993, RRID: AB_10864916), rabbit anti-HSP60 (1:1000, Abcam Cat# ab190828, RRID: AB_2814692), rabbit anti-**PERK** (1:1000, Abcam Cat# ab229912, RRID: AB_2941805), rabbit anti-**IRE1α** (1:1000, Abcam Cat# ab37073, RRID: AB_775780), rabbit anti-**GRP78** (1:1000, Abcam Cat# ab21685, RRID: AB_2119834), mouse anti-CHOP (1:1000, Abcam Cat# ab11419, RRID: AB_298023), rabbit anti-HA (1:1000, Abcam Cat# ab9110, RRID: AB_307019), rabbit anti-p-IκBα (1:1000, Abcam Cat# ab92700, RRID: AB_10562951), rabbit anti-IκBα (1:1000, Abcam Cat# ab32518, RRID: AB_733068), rabbit anti-p-p65 (1:1000, Abcam Cat# ab76302, RRID: AB_1524028) and rabbit anti-p65 (1:1000, Abcam Cat# ab16502, RRID: AB_443394) were obtained from Abcam (Cambridge, UK). The secondary antibody goat anti-mouse IgG H&L (1:1000, Biodragon Cat# BF03001, RRID: AB_3105782) and goat anti-rabbit IgG H&L (1:1000, Biodragon Cat# BF03008, RRID: AB_3073988) were purchased from Biodragon (Jiangsu, China). The APC-conjugated monoclonal mouse **CD86** antibody (1:50, BioLegend Cat# 159215, RRID: AB_3106041) and APC-conjugated monoclonal mouse CD206 antibody (1:50, BioLegend Cat# 141708, RRID: AB_10900231) were purchased from BioLegend.

2.2 | Nef-probe synthesis

(S)-1-(4-(2-(3-(But-3-yn-1-yl)-3H-diazirin-3-yl)ethoxy)-3-(((R)-6--methoxy-1-(4-methoxybenzyl)-2-methyl-1,2,3,4--tetrahydroisoquinolin-7-yl)oxy)benzyl)-6,7-dimethoxy-2--methyl-1,2,3,4-tetrahydroisoquinoline

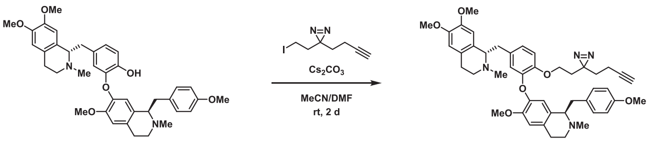

The chemical transformation was conducted under light-protected conditions. A 10-ml reaction vessel was charged with Nef (49.9 mg, 0.08 mmol), 3-(but-3-yn-1-yl)-3-(2-iodoethyl)-3H-diazirine (20 μl, 0.16 mmol) and caesium carbonate (52 mg, 0.16 mmol), which were subsequently dissolved in 2 ml of an acetonitrile/dimethylformamide mixed solvent system (1:1, v/v). The resultant mixture underwent continuous agitation at ambient temperature for 48 h. Following reaction termination through aqueous quenching (50 ml H_2O), the mixture underwent sequential dichloromethane extractions (3 × 15 ml). The collected organic phases were successively washed with deionized water and saturated sodium chloride solution and then dehydrated using anhydrous sodium sulphate. After filtration through medium-porosity filter paper, solvent elimination was achieved via rotary evaporation under vacuum conditions. Final purification of the crude material was accomplished by preparative thin-layer chromatography employing a dichloromethane/methanol mobile phase (50:1 v/v) (S2, S3 and S4).

^{1}H NMR (600 MHz, $CDCl_3$) δ 6.97–6.87 (m, 2H), 6.79 (d, $J = 8.2$ Hz, 1H), 6.76–6.70 (m, 1H), 6.70–6.58 (m, 4H), 6.51 (s, 1H), 6.21 (s, br, 1H), 6.02 (s, br, 1H), 4.00–3.63 (m, 13H), 3.58 (s, 3H), 3.30–3.12 (m, 3H), 3.12–3.00 (m, 1H), 2.93–2.72 (m, 6H), 2.72–2.59 (m, 2H), 2.52 (s, 6H), 2.03–1.90 (m, 3H), 1.82–1.66 (m, 2H), 1.62–1.52 (m, 2H).

^{13}C NMR (151 MHz, $CDCl_3$) δ 157.9, 148.8, 147.9, 147.6, 146.6, 146.0, 144.1, 130.4, 125.3, 120.9, 117.5, 114.6, 113.5, 112.2, 111.2, 110.9, 82.9, 69.1, 64.8, 64.4, 64.0, 55.9, 55.8, 55.7, 55.1, 47.0, 46.5, 42.2, 40.5, 40.0, 33.1, 32.5, 26.7, 25.3, 24.7, 13.2.

HRMS found: *m/z*: 745.3967 $[M + H]^+$, calcd. for $C_{45}H_{53}N_4O_6^+$, 745.3960.

2.3 | Cell culture

Mouse microglial cells (BV2, RRID: CVCL_0182) and HEK293T (RRID: CVCL_0063) cells were acquired from the Cell Bank of Peking Union Medical College. Cellular maintenance involved propagation in Dulbecco's modified eagle medium (DMEM) formulated with 10% (v/v) heat-inactivated fetal bovine serum, along with antibiotic supplementation consisting of 100 μg ml^{-1} streptomycin and 100 U ml^{-1} penicillin. Standard culture conditions comprised continuous incubation at 37°C within a humidified chamber regulated at 5% CO_2 concentration.

2.4 | Nitric oxide (NO) analysis

BV2 cells were treated with **LPS** (1 μg ml^{-1}) and Nef (2.5, 5 and 10 μM) for 24 h. NO production was measured using the NO detection kit (Jiancheng, Nanjing, Jiangsu, China). The cell supernatant was collected and incubated with Griess reagent at a ratio of 1:1 at 25°C for 10 min. The intensity of dye was measured spectrophotometrically at 550 nm with Tecan E Plex absorbance measurement system (Tecan, Bern, Switzerland). The absorbance was then correlated with a standard curve generated using known concentrations of nitrite, allowing for the quantification of **NO** levels.

2.5 | Cell viability analysis

Cell viability was analysed by employing the MTT solution. BV2 cells were subjected to treatment with LPS (1 μg ml^{-1}) in the presence of Nef (2.5, 5 and 10 μM). After completion of a 24-h incubation period, cellular supernatants were carefully removed by aspiration followed by administration of MTT-based staining reagent (500 μg ml^{-1}) to each cellular compartment. The biological specimens were then maintained under light-protected conditions at physiological temperature (37°C) for 4 h metabolic conversion interval. The resultant formazan deposits underwent solubilisation through dimethyl sulfoxide (DMSO) addition, with subsequent spectrophotometric quantification of optical density at 570 nm wavelength employing a Tecan E Plex absorbance measurement system (Tecan Group AG, Switzerland).

2.6 | Quantitative real-time PCR analysis

Total RNA isolation was conducted with the MolPure Cell/Tissue Total RNA Purification System (YEASEN Biotechnology, Shanghai, China). Complementary DNA synthesis was subsequently achieved through reverse transcription employing the Hifair III First-Strand cDNA Preparation SuperMix (YEASEN Biotechnology, Shanghai, China). Quantitative analysis of gene expression was performed via SYBR Green-based real-time PCR methodology using the Hieff qPCR Fluorescent Detection Master Mix (YEASEN Biotechnology, Shanghai, China). The amplification system was formulated as 20 μl reactions containing SYBR Green detection chemistry (10 μl), cDNA template (2 μl), primer pairs (200 nM final concentration) and RNase-free water to adjust volume. The primer sequences used for RT-qPCR were presented in Table 1. Thermal cycling was executed on a Roche LightCycler 96 real-time PCR platform (Roche Diagnostics GmbH, Basel, Switzerland). β-Actin housekeeping gene transcripts served as endogenous normalisation controls.

2.7 | Flow cytometry analysis

BV2 cells were seeded in six-well dishes at a density of 1×10^6 cells per well and then treated with LPS (1 μg ml^{-1}) along with Nef (2.5, 5 and 10 μM) for 24 h. The cells were collected and washed in cold PBS. Quantitative surface marker profiling was performed via direct immunofluorescence assay targeting CD86 and CD206 membrane antigens. Cellular specimens were exposed to APC-labelled murine-derived monoclonal immunoreagents specific for CD86 or CD206 under light-protected ambient conditions (25°C, 30 min). Post-staining procedures involved dual PBS washing cycles followed by final resuspension in 500 μl phosphate-buffered saline. Cellular fluorescence intensity quantification was achieved through CytoFLEX flow cytometric analysis (Beckman Coulter Life Sciences Division, CA, USA) with 10^4 events acquired per experimental condition.

2.8 | Cell painting analysis

BV2 cells were plated in 96-well dishes at a density of 5×10^3 per well and treated with LPS (1 μg ml^{-1}) and Nef (2.5, 5 and 10 μM) for 24 h. The cell painting dyes included: Hoechst 34580 (DNA/nucleus), **concanavalin A**, Alexa Fluor™ 488 Conjugate (ER), SYTO14 (RNA, nucleolus), Alexa Fluor™ 568 Phalloidin (F-actin), Wheat Germ Agglutinin, Alexa Fluor™ 555 Conjugate (Golgi) and MitoTracker™ Deep Red FM (mitochondria). Plates were imaged on a Yokogawa CV8000 high-throughput spinning disk confocal microscope (Yokogawa Electric Corporation, Tokyo, Japan) with sequential imaging of the six cell painting channels. Image analysis was performed utilising CellPathfinder (Yokogawa Electric Corporation, Tokyo, Japan) to compensate for illumination inhomogeneity, spatial registration discrepancies across imaging detectors and spectral bleed-through between fluorescent channels. For each experimental campaign, no fewer than nine distinct fields of view were captured per biological sample well.

2.9 | TPP experiment

BV2 cells were cultured using the Stable Isotope Labeling with Amino acids in Cell culture (SILAC) to incorporate stable isotopes into cellular

TABLE 1 Primers for RT-qPCR.

Gene	Forward (5′–3′)	Reverse (5′–3′)
Inos	GTTCTCAGCCCAACAATACAAGA	GTGGACGGGTCGATGTCAC
Tnf-α	CAGGCGGTGCCTATGTCTC	CGATCACCCCGAAGTTCAGTAG
Il-1β	GAAATGCCACCTTTTGACAGTG	TGGATGCTCTCATCAGGACAG
Il-4	CCCCAGCTAGTTGTCATCCTG	CAAGTGATTTTTGTCGCATCCG
Il-10	CTTACTGACTGGCATGAGGATCA	GCAGCTCTAGGAGCATGTGG
B-actin	GTGACGTTGACATCCGTAAAGA	GCCGGACTCATCGTACTCC

proteins. Specifically, two distinct populations of BV2 cells were grown in DMEM supplemented with either $^{12}C_6{}^{14}N_2$-lysine and $^{12}C_6$ $^{14}N_4$-arginine (light-label medium) or $^{13}C_6{}^{15}N_2$-lysine and $^{13}C_6{}^{15}N_4$-arginine (heavy-label medium). This process was continued for more than six cell generations to ensure that the incorporation of heavy-labelled arginine and lysine reached a level of over 95%. BV2 cells cultured in heavy-labelled medium were treated with LPS (1 μg ml^{-1}) and Nef (10 μM) for 3 h. In parallel, BV2 cells cultured in light-labelled medium were treated with LPS (1 μg ml^{-1}) and DMSO for the same period. Both the heavy-labelled and light-labelled BV2 cells were subjected to a heat shock at 55°C for 3 min. The cells were lysed to extract total cellular proteins. The lysates from the light-labelled and heavy-labelled BV2 cells were mixed in a 1:1 ratio. Proteins were identified by LC-MS/MS. Data were considered valid if the target was detected in at least three out of five independent experimental replicates by mass spectrometry.

2.10 | LC-MS/MS analysis

Liquid chromatography in tandem with an LTQ Velos pro mass spectrometer (Waltham, MA, USA) was employed to analyse the trypsin-digested samples. Samples were initially loaded onto a trapping column packed with 5 μm C18 reversed-phase media, followed by peptide separation on an analytical column containing the same stationary phase. The gradient program consisted of three phases: 2%–40% solvent B (0.1% formic acid in acetonitrile) over 70 min, 40%–95% B in 5 min, and 95% B maintained for 20 min, with solvent A being 0.1% formic acid in water. Chromatographic separation occurred at a constant flow rate of 300 nl min^{-1} into the mass spectrometer. Mass spectrometry analysis was performed under the following conditions: 35% HCD collision energy, 60,000 resolution, 50 ms maximum injection time, and m/z 350–2000 scan range. Peptide spectral matches were filtered at 1% strict false discovery rate. Proteomic data processing was completed using Proteome Discoverer 1.4 software with the integrated SEQUEST algorithm.

2.11 | Protein expression and purification

The human BAP31 full-length clone was used as template for PCR amplification of its C-terminal cytoplasmic domain (residues 124–242). The amplified DNA fragment was inserted into a modified pET28a vector to generate an N-terminal 6 × His-tagged construct. The recombinant plasmid was transformed into *Escherichia coli* BL21(DE3) cells. Bacterial cultures were grown in LB medium at 37°C until reaching OD600 = 0.8, followed by overnight induction with 0.5 mM IPTG at 16°C. Cells from 500 ml culture were harvested and resuspended in 25 ml lysis buffer (20 mM HEPES, 250 mM NaCl, 10% glycerol, pH 7.5). After sonication and lysate centrifugation, the soluble fraction was filtered and loaded onto Ni-NTA resin. The column underwent gradient imidazole washes, with target protein eluting at 250 mM imidazole. Purified protein was concentrated to 10 mg ml^{-1} and cryopreserved at −80°C.

2.12 | Surface plasmon resonance (SPR) analysis

The interactions between Nef and BAP31 (amino acids 124–242) were evaluated by a Biacore 8K+ system at 25°C (Cytiva, Marlborough, MA, USA). Recombinant BAP31 (amino acids 124–242) was immobilised onto an activated CM5 sensor chip. Specifically, the carboxyl groups on the surface of the chip were activated with a mixture of EDC and NHS. The primary amines of the protein were conjugated to the activated chip, utilising a running buffer composed of PBS containing 0.05% (v/v) Tween 20 and 5% (v/v) DMSO. Nef was then injected over the immobilised BAP31 at a flow rate of 30 μl min^{-1}, with a gradient of concentrations being employed to determine the binding affinity and kinetics. The results were analysed using the Biacore Evaluation software (Cytiva, Marlborough, MA, USA). The acquired data were fitted to a 1:1 l binding model, which presupposed a straightforward bimolecular interaction between the Nef and BAP31.

2.13 | Microscale thermophoresis (MST) assay

HEK293T cells were transfected with the pEGFP-N1-BAP31 plasmid. After 48 h, cells were collected and lysed. A series of Nef concentrations (0, 0.008, 0.015, 0.03, 0.06, 0.12, 0.24, 0.49, 0.98, 1.95, 3.9, 15.6, 62.5, 125 and 250 μM) were prepared and incubated with the cell lysate in a buffer containing 5% DMSO and 0.05% Tween 20 in PBS at 25°C for 10 min. 10 μl of each sample were transferred to glass capillaries (Nano Temper, Munich, Germany). The thermophoresis of BAP31 in the presence of Nef was measured using the Nano Temper Monolith Instrument (Nano Temper, Munich, Germany). The results were analysed using the MO. Affinity Analysis software (Nano Temper, Munich, Germany) to determine the binding affinity.

2.14 | Cellular thermal shift assay (CETSA)

The experimental procedure involved incubating BV2 cells with either 10 μM Nef solution or DMSO control for a 3-h period. Post-treatment cellular samples were partitioned into aliquots and exposed to sequential thermal stress at incremental temperatures (43–67°C), maintaining each elevated temperature condition for 3 min. Post-heating specimens were gradually equilibrated to ambient temperature. Cellular disruption was achieved through cryogenic processing involving eight alternating cycles of liquid nitrogen immersion (freezing phase) and ambient temperature recovery (thawing phase). The resultant lysates underwent refrigerated centrifugation at 12,000 rpm for 15 min to segregate soluble components from particulate matter. Supernatant fractions enriched with soluble proteins were carefully harvested for downstream applications. Protein characterisation was ultimately performed through immunoblotting analysis.

2.15 | Transient transfection

HEK293T and BV2 cells were seeded at a density of approximately 70% confluence on the day of transfection. For the transfection of plasmids or siRNA, Opti-MEM medium was utilised in conjunction with either Lipofectamine 2000 or Lipofectamine RNAiMAX reagents (Thermo Fisher Scientific, Waltham, MA, USA). Then, the cells were incubated with the transfection complexes for 6 h. Following the incubation, the transfection medium was replaced with complete growth medium. The cells were harvested for subsequent analyses after 48 h.

2.16 | Bimolecular fluorescence complementation (BiFC) assay

Plasmids were constructed by fusing the N-terminal (VN) and C-terminal (VC) fragments of the Venus fluorescent protein to the C-terminus of the BAP31 protein, resulting in two constructs: BAP31-VN and BAP31-VC. These constructs allowed for the reconstitution of the full Venus protein. HEK293T cells were seeded in six-well plates and transfected with the BAP31-VN and BAP31-VC constructs. For the BiFC assay, cells were co-transfected with both constructs at a 1:1 ratio. 48 h post-transfection, the cells were treated with different concentrations of Nef or Arm for a specified time. Before detecting fluorescence intensity, the medium was replaced with PBS. Fluorescence quantification of Venus was performed with a microplate reader (Tecan E Plex; manufactured in Bern, Switzerland). The system parameters included excitation at 485 nm and emission detection at 535 nm.

2.17 | Crosslinking assay

Recombinant BAP31 (amino acids 124–242) was prepared at a concentration of 80 μg ml^{-1}. The protein was incubated with varying concentrations of Nef or Arm (0, 10, 20, 50, 100 and 200 μM) at room temperature for 2 h. Following incubation, the protein mixtures were treated with 0.05% glutaraldehyde at room temperature for 10 min to crosslink proteins. The crosslinking reaction was subsequently quenched by adding 20 mM Tris–HCl, pH 7. The crosslinked protein samples were ultimately performed through immunoblotting analysis.

2.18 | Western blotting assay

All immuno-related procedures used comply with the recommendations made by the *British Journal of Pharmacology* (Alexander et al., 2018). The protein isolation from cellular material was performed through RIPA lysis buffer containing protease and phosphatase inhibitors. Subsequent electrophoretic separation was conducted using sodium dodecyl sulfate–polyacrylamide gel electrophoresis (SDS-PAGE) under denaturing conditions. Following electrophoretic migration, the protein components were transferred onto polyvinylidene fluoride (PVDF) membranes with 0.22 μm porosity through semi-dry transfer methodology. Membranes were subjected to blocking solution consisting of 5% (w/v) non-fat dried milk dissolved in Tris-buffered saline containing 0.1% Tween 20 (TBST) for 60 min at ambient temperature. Immunoblotting procedures involved sequential incubations: primary antibody exposure was maintained at 4°C for 16 h, followed by three 10-min TBST washing cycles prior to 2-h room temperature incubation with horseradish peroxidase (HRP)-conjugated secondary antibodies. Protein-antibody complexes were subsequently detected using the Tanon 5200 chemiluminescence imaging system (Tanon, Shanghai, China). Quantitative analysis of immunoreactive bands was performed through densitometric measurements using ImageJ software.

2.19 | Ascorbate peroxidase 2 (APEX2) proximity labelling analysis

HEK293T cells were transfected with Flag-BAP31-APEX2 plasmid and incubated for 48 h before treatment with biotin-phenol (500 μM) and Nef (10 μM) at 37°C for 4 h, followed by 1 mM H_2O_2 exposure for 60 s to activate APEX2 peroxidase activity. The reaction was terminated via triple washing with quenching buffer (PBS containing 10 mM sodium azide, 10 mM sodium ascorbate and 5 mM Trolox), after which cells were lysed in RIPA buffer supplemented with protease inhibitors and centrifuged to remove insoluble debris. Protein homogenates with normalised concentrations underwent 6-h affinity purification at 4°C using streptavidin-conjugated beads, followed by sequential washing with RIPA buffer, high-salt Tris–HCl (pH 7.0, 1 M KCl), urea-enriched alkaline solution (0.1 M Na_2CO_3, 2 M urea) and a final RIPA rinse. Captured proteins were subjected to tryptic digestion, and the resulting peptides were identified through LC-MS/MS spectral analysis. Data were considered valid if the target was detected in at least three out of five independent experimental replicates by mass spectrometry.

2.20 | Co-immunoprecipitation (Co-IP) assay

HEK293T cells were transiently transfected with a plasmid carrying HA-BAP31. Following 48 h of transfection, the cells underwent Nef treatment (10 μM) through 4-h incubation at 37°C. Post-treatment cellular samples were harvested and lysed using RIPA buffer containing protease inhibitors. Lysates were clarified by centrifugation (12,000 rpm, 15 min, 4°C) to eliminate particulate matter. Clarified supernatants with equalised protein quantities were incubated with HA-affinity beads at 4°C for 6 h. Non-bound proteins were subsequently removed through sequential washing with a PBS-based elution buffer containing 0.1% Triton X-100. Immunoblotting analysis was performed on captured proteins using antigen-specific antibodies.

2.21 | RNA sequencing assay

BV2 cells were treated with LPS (1 μg ml^{-1}) and Nef (10 μM) for 24 h. The cells were washed twice with PBS pre-warmed to 37°C, and the PBS was subsequently discarded. A volume of 35 μl of lysis buffer (prepared by supplementing 1 ml of lysis buffer with 12.5 μl of RNase inhibitor) was added to each well. Processed samples were temporarily stored at −80°C until further processing. Library preparation was performed according to the DRUG-Seq2 protocol, wherein barcodes were incorporated during reverse transcription to enable sample-specific labelling. Sequencing was conducted by a commercial sequencing service using the Illumina NovaSeq platform. Sequencing fragments were converted into sequence data (reads) via Casava base calling. The sequencing data were divided into two files: R1 and R2. The R1 file contained sequences with a 10-nucleotide cell identification barcode and a 10-nucleotide unique molecular identifier (UMI), while the R2 file encompassed transcript sequencing information. Barcode and UMI information were extracted from the R1 file, and erroneous barcodes were filtered using a predefined barcode list. The proportion of valid barcodes was calculated, and an updated R2 file containing barcode and UMI annotations was generated. Cutadapt was employed to remove adapter sequences and low-quality bases, yielding clean reads and a FastQC quality control report. Clean reads were aligned to the reference genome using STAR, and gene quantification was performed with featureCounts by counting reads mapped to exonic regions. The resulting expression matrix was processed and analysed using the Seurat software package.

2.22 | Stimulated emission depletion microscope (STED) analysis

BV2 cells were plated in glass bottom dishes at a density of 2×10^5 per well. After 12 h, cells were treated with LPS (1 μg ml^{-1}) and Nef (10 μM) for 6 h. The cells were stained with PKMITO (2 μM) at 37°C for 20 min, washed three times with PBS and immediately imaged. For stimulated emission depletion microscope (STED) imaging, the images of fixed samples were acquired using a STELLARIS 8 FALCON microscope (Leica, Wetzlar, Germany). The images were captured with an SR Apo TIRF 100 × 1.49 N.A. oil objective. PKMITO was excited at 561 nm wavelength, and STED was performed using a pulsed depletion laser at 775 nm wavelength.

2.23 | Neuroinflammation mouse model

C57BL/6 mice (6–8 weeks, 20–25 g) were obtained from the Department of Laboratory Animal Science, Peking University Health Science Center. The mice were maintained under specific pathogen-free conditions with a 12-h light/dark cycle. They had free access to water and standard chow and were kept in cages of uniform dimensions with wood shavings as bedding material. All care and treatment of the experimental animals were conducted in strict accordance with the guidelines of the Laboratory Animal Care Assessment and Accreditation Association of Peking University, approved by the Institutional Animal Care and Use Committee of Peking University (Licence no. DLASBD0495). Animal studies are reported in compliance with the ARRIVE guidelines (du Sert et al., 2020) and with the recommendations made by the *British Journal of Pharmacology* (Lilley et al., 2020). Mice were randomly divided into four groups: control group, LPS model group (5 mg kg^{-1}) and Nef treatment groups (10 and 50 mg kg^{-1}). All mice received daily oral gavage administration for three consecutive days, with the Nef treatment groups receiving Nef suspension while the control and LPS model groups received 0.5% CMC-Na. On the fourth day, mice in the LPS model group and Nef treatment groups were intraperitoneally injected with LPS at 5 mg kg^{-1}, whereas the control group received equivalent physiological saline. At 24 h post-LPS injection, mice were anaesthetised via inhalation of **isoflurane** (2% concentration vaporised at 0.41 ml min^{-1} with 4 l min^{-1} fresh gas flow) and subsequently euthanised by cervical dislocation; sacrifice was confirmed through comprehensive assessment including cessation of pulse and respiration, pupillary dilation, absence of corneal reflex and loss of toe pinch withdrawal reflex prior to tissue collection for subsequent analyses.

2.24 | MCAO mouse model

C57BL/6 mice (6–8 weeks, 20–25 g) were obtained from the Department of Laboratory Animal Science, Peking University Health Science Center. The mice were maintained under specific pathogen-free conditions with a 12-h light/dark cycle. They had free access to water and standard chow and were kept in cages of uniform dimensions with wood shavings as bedding material. All care and treatment of the experimental animals were conducted in strict accordance with the guidelines of the Laboratory Animal Care Assessment and Accreditation Association of Peking University, approved by the Institutional Animal Care and Use Committee of Peking University (Licence no. DLASBD0236). Animal studies are reported in compliance with the ARRIVE guidelines (du Sert et al., 2020) and with the recommendations made by the *British Journal of Pharmacology* (Lilley et al., 2020). Following anaesthesia with isoflurane (2% concentration vaporised at 0.41 ml min^{-1} with 4 l min^{-1} fresh gas flow), mice were placed in a supine position on a surgical platform and securely immobilised. The ventral cervical region, spanning from the mandible to the clavicle, was shaved and disinfected with povidone-iodine. A midline longitudinal incision (2–3 cm in length) was created along the neck. Blunt dissection with haemostatic forceps was performed to separate the cervical musculature, exposing the right common carotid artery (CCA), external carotid artery (ECA) and internal carotid artery (ICA). The CCA and ICA were temporarily occluded using vascular clamps. The proximal segment of the ECA was ligated with surgical silk, and a small incision was made distal to the ligation site. A 3-0 nylon monofilament (tip heat-rounded to form a smooth bulb) was introduced into the ECA lumen and gently advanced through the CCA bifurcation into the ICA. The filament was further advanced until mild resistance was encountered, indicating occlusion of the middle cerebral artery (MCA) origin to induce focal cerebral ischaemia. Successful vascular occlusion was confirmed, and the filament was secured in place. Vascular clamps were subsequently removed, and muscular and cutaneous layers were sutured. Mice were maintained in a thermoregulated environment (37°C). After 1 h of ischaemia, the filament was carefully withdrawn to restore cerebral reperfusion. Sham-operated controls underwent identical procedures excluding filament insertion. Postoperatively, mice (excluding sham controls) were randomly allocated into four groups: MCAO model group, Nef-treated groups (10 and 50 mg ml^{-1}) and positive control group (**nimodipine**, 20 mg ml^{-1}). Oral gavage administration commenced 12-h post-surgery and continued for 4 consecutive days. Nef-treated groups received a suspension of Nef, whereas sham and MCAO model groups received 0.5% CMC-Na vehicle. The positive control group received nimodipine. At 4 days post-treatment, all mice were euthanised under isoflurane anaesthesia (2% concentration vaporised at 0.41 ml min^{-1} with 4 l min^{-1} fresh gas flow), followed by cervical dislocation; sacrifice was confirmed through multimodal assessment including cessation of spontaneous respiration and heartbeat, pupillary dilation, absence of corneal reflex and loss of toe pinch withdrawal reflex prior to tissue harvesting for subsequent analyses.

2.25 | Neurological deficit evaluation

The Zea-Longa scoring system, which ranges from 0 to 4, was utilised for estimating cerebral injury after MCAO. The scoring criteria are as follows: 0 indicates no apparent neurological deficits, 1 indicates the inability to extend the affected forelimb, 2 indicates walks in circles, 3 indicates unbalanced walking, and 4 indicates numbness and inability to walk.

2.26 | TTC staining analysis

The brains were extracted and subsequently sliced into 2 mm sections. The sections were immersed in a 1% TTC working solution at 37°C for 30 min and then placed in 10% formaldehyde. Subsequently, the sections were photographed by a digital camera and the images were quantified using the image analysis software ImageJ. The infarct area of each section was documented.

2.27 | Nissl staining assay

Mouse brains were immediately placed in 4% paraformaldehyde fixative solution and fixed for 24 h to preserve tissue morphology and antigenicity. The fixed tissues were sequentially dehydrated through graded ethanol concentrations, cleared with xylene and embedded in paraffin to form tissue blocks. Using a microtome, the tissue blocks were sectioned into 3-μm-thick slices and mounted onto glass slides. The sections were deparaffinised by immersion in xylene, followed by rehydration through a graded ethanol series and finally rinsed three times with distilled water. The sections were stained with 1% toluidine blue solution for 40 min and then rinsed with distilled water. After staining, the sections were dehydrated through a graded ethanol series and cleared in xylene for 10 min. Neutral resin was applied to the sections, which were then covered with coverslips. The mounted sections were air-dried at room temperature prior to microscopic observation and image acquisition. Sections were imaged with a digital slide scanner Nanozoomer-SQ (Hamamatsu Photonic, Hamamatsu, Japan).

2.28 | Immunohistochemical analysis

All immuno-related procedures used comply with the recommendations made by the *British Journal of Pharmacology* (Alexander et al., 2018). Brains were immediately immersed in 4% paraformaldehyde fixative and fixed for 24 h to preserve tissue morphology and antigenicity. The fixed tissues were sequentially dehydrated through a graded ethanol series, cleared in xylene and embedded in paraffin to create tissue blocks. Using a microtome, the blocks were sectioned into 3-μm-thick slices and mounted onto glass slides. For deparaffinisation, the sections were immersed in xylene, followed by rehydration through a descending ethanol series (100%, 95%, 80%, 70%). After three washes with PBS, excess liquid was gently removed, and blocking solution was applied to cover the sections. These were incubated at 25°C for 30 min to block non-specific binding sites. Following blocking solution removal, diluted primary antibody solution was directly applied to the sections and incubated overnight at 4°C. Subsequently, diluted secondary antibody solution was added and incubated at 25°C for 1 h. For chromogenic detection, DAB working solution was applied, and colour development proceeded at for 15 min. The sections were then dehydrated through an ascending ethanol series, cleared in xylene for 10 min and mounted with neutral resin under coverslips. After air-drying, the prepared slides were ready for microscopic observation and imaging. Sections were imaged with a digital slide scanner Nanozoomer-SQ (Hamamatsu Photonic, Hamamatsu, Japan).

2.29 | Data and analysis

The experimental procedures and statistical methods adhered to the guidelines provided by the *British Journal of Pharmacology* concerning experimental design and analysis in pharmacology (Curtis et al., 2025). The study design aimed to achieve groups of equal size through randomisation and blinded assessment. In this study, animal experiments were designed with equal group sizes ($n = 6$/group) and randomly assigned. Investigators conducting behavioural assessments and histological analyses were blinded to group allocation throughout data collection and processing to minimise experimenter bias. Statistical evaluations were performed exclusively for experiments where every group contained a minimum of $n = 5$ independent replicates. For studies falling below the threshold of $n < 5$, data are reported as exploratory observations only, with no inferential statistics applied. The stated group size corresponds to the number of independent observations, and all statistical tests were conducted based on these independent values. Group sizes were determined via a priori power analysis ($a = 0.05$, $\beta = 0.8$) using GPower3.1. No outliers were detected in any of the experiments presented, and no data points were omitted from the analyses. The control group values were normalised to '1', and all test group values are expressed as relative fold changes compared to the control. Accordingly, the Y axis in the figures is designated as 'fold mean of the controls' following data transformation. Data were presented in the form of mean ± SD. They were analysed using GraphPad Prism version 8.0 (GraphPad Software, La Jolla, CA, USA). For comparisons involving more than two groups, a one-way ANOVA was applied to evaluate intergroup differences, whereas an unpaired *t*-test was used for comparisons between two groups. Data normalisation was performed to minimise undesired variations. Post hoc analyses were conducted only when the F reached a significance level of $P < 0.05$ and no significant heterogeneity of variance was observed. A *P*-value below 0.05 was regarded as statistically significant for differences in mean values across groups.

2.30 | Nomenclature of targets and ligands

Key protein targets and ligands in this article are hyperlinked to corresponding entries in https://www.guidetopharmacology.org, and are permanently archived in the Concise Guide to PHARMACOLOGY 2021/2022 (Alexander et al., 2021).

3 | RESULTS

3.1 | Nef promotes the M1-to-M2 polarisation in LPS-induced BV2 cells

Nef is a naturally derived alkaloid (Figure 1a), with a wide range of pharmacological activity. In this study, we observed that Nef significantly inhibited the release of NO in BV2 cells induced by LPS (Figure 1b). Moreover, Nef did not exhibit significant cytotoxicity (Figure 1c). The concentrations of Nef (2.5, 5 and 10 μM) employed in this study were selected based on substantial literature evidence demonstrating potent anti-inflammatory efficacy within the 1–30 μM range across diverse cell types, coupled with a favourable safety profile at concentrations ≤10 μM, a non-toxic therapeutic window further confirmed in our BV2 microglia model where Nef concentration-dependently suppressed LPS-induced NO release without compromising cell viability. Then, we assessed whether Nef regulated the expression of inflammatory mediators with RT-PCR. The results showed that LPS increased the gene expressions of M1 pro-inflammatory markers including **iNOS**, **TNF-α** and **IL-1β**, which was significantly reversed by Nef (Figure 1d–f). Moreover, Nef obviously increased the gene expressions of M2 anti-inflammatory markers such as **IL-4** and **IL-10** (Figure 1g,h). Next, we evaluated the effect of Nef on the phenotypic conversion of BV2 cells by measuring the M1 polarisation marker CD86 and the M2 polarisation marker CD206 by flow cytometry analysis. Compared to the LPS group, the CD86 expression was significantly down-regulated following Nef treatment (Figure 1i). Conversely, Nef treatment increased the level of CD206 in BV2 cells compared to the LPS group (Figure 1j). Additionally, we conducted a comprehensive investigation into the effects of Nef on the morphological changes of various organelles during the polarisation transition from M1 to M2 in microglial cells, utilising a cell painting analysis. As shown in Figure 1k, we observed that Nef significantly altered the fluorescence intensities of the Golgi, ER and mitochondria (Figure 1l), indicating that the function of these organelles was potentially affected by Nef. Therefore, these results indicate that Nef exhibits obvious anti-inflammatory effects in LPS-stimulated BV2 cells by inducing the transformation from M1 to M2 polarisation.

3.2 | B-cell receptor-associated protein 31 (BAP31) is identified as a direct cellular target of Nef

We next employed the thermal proteome profiling (TPP) method to identify the potential cellular targets of Nef in BV2 cells (Figure 2a). Cells were treated with Nef or DMSO respectively for 3 h. Then, the cells were collected and heated at 55°C for 3 min. Native proteins exhibit lower thermal stability compared to their ligand-bound forms, a principle that guided our selection of 55°C as the optimal temperature for TPP experiments in identifying Nef's cellular targets. At physiological temperature (37°C), protein denaturation is minimal, whereas temperatures above 60°C led to excessive aggregation and loss of measurable signals, underscoring the importance of an intermediate thermal challenge that effectively differentiates ligand-stabilised proteins from their unbound counterparts whilst preserving experimental robustness and reproducibility. Following repeated freeze–thaw cycles, the samples were analysed via mass spectrometry. Through LC-MS/MS analysis, we identified a total of 1697 Nef-binding proteins. Then, we screened the protein list and focused on 25 proteins exhibiting a fold change greater than 2 and a *P*-value exceeding 0.05. Further analysis of biological functions led to the selection of eight

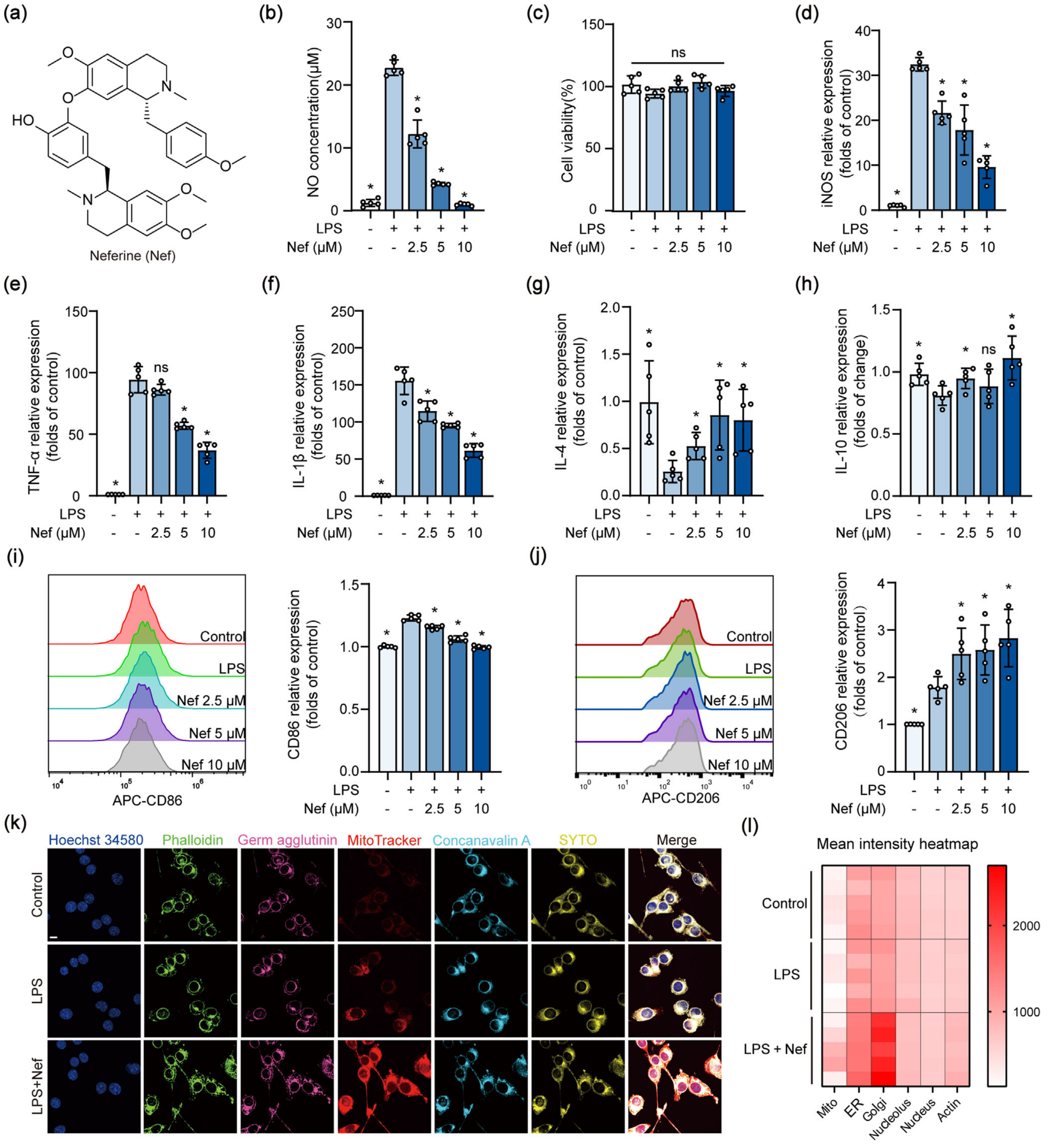

FIGURE 1 **Nef promotes the M1-to-M2 polarisation of microglia.** (a) The chemical structure of Nef. (b) Nef inhibited NO production from BV2 cells. Cells were treated with LPS (1 μg ml^{-1}) and Nef (2.5, 5 and 10 μM) for 24 h. n = 5. (c) MTT assay for cell viability after Nef treatment. Cells were treated with LPS (1 μg ml^{-1}) and Nef (2.5, 5 and 10 μM) for 24 h. n = 5. (d–f) Nef inhibited LPS-induced iNOS, TNF-α and IL-1β mRNA expression by RT-PCR in BV2 cells. Cells were treated with LPS (1 μg ml^{-1}) and Nef (2.5, 5 and 10 μM) for 6 h. n = 5. (g,h) Nef promoted LPS-induced IL-4 and IL-10 mRNA expression by RT-PCR in BV2 cells. Cells were treated with LPS (1 μg ml^{-1}) and Nef (2.5, 5 and 10 μM) for 6 h. n = 5. (i) Effect of Nef on LPS-induced protein expression of CD86 in BV2 cells was measured by flow cytometry. Cells were treated with LPS (1 μg ml^{-1}) and Nef (2.5, 5 and 10 μM) for 24 h. n = 5. (j) Effect of Nef on LPS-induced protein expression of CD206 in BV2 cells was measured by flow cytometry. Cells were treated with LPS (1 μg ml^{-1}) and Nef (2.5, 5 and 10 μM) for 24 h. n = 5. (k) Cell painting analysis of BV2 cells. Cells were treated with LPS (1 μg ml^{-1}) and Nef (10 μM) for 24 h. Scale bar, 10 μm. n = 5. (l) Heatmap of average fluorescence intensity of organelles after cell painting result analysis. *$P < 0.05$, significantly different from model group; ns, no significant difference.

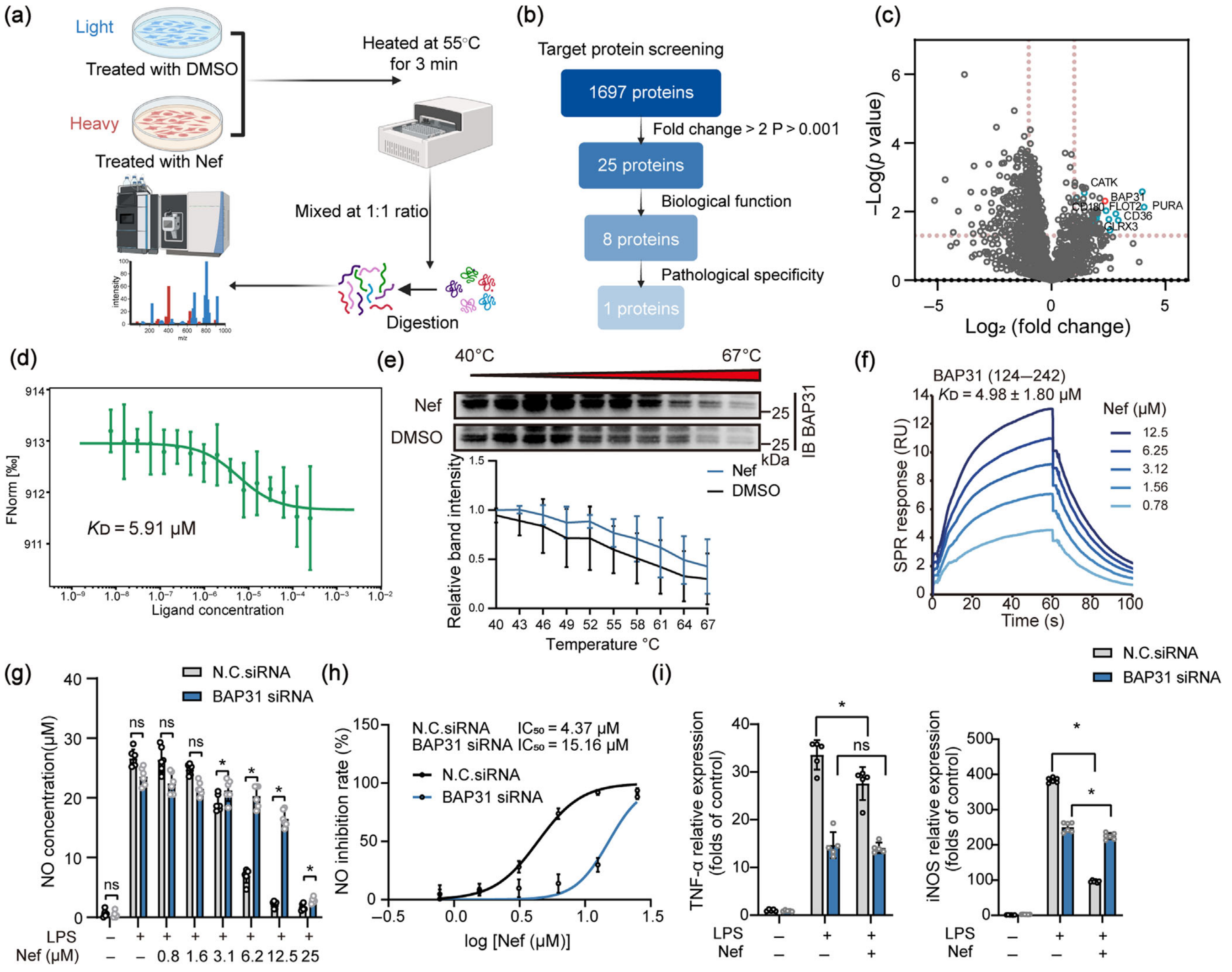

FIGURE 2 **BAP31 is a direct cellular target of Nef.** (a) Flow diagram of TPP coupled with SILAC for target identification in BV2 cells. (b) Schematic diagram of the target screening process. (c) Volcano plots of cellular targets by the TPP strategy. (d) The binding of Nef to BAP31 was determined by microscale thermophoresis (MST). n = 5. (e) Cellular thermal shift assay (CETSA) was performed using the cells exposed to Nef (10 μM). n = 5. (f) SPR assay of Nef with the truncated variant of BAP31 (amino acids 124–242). n = 5. (g) BAP31 knockdown reversed Nef-mediated inhibition of LPS-induced NO. Cells were treated with LPS (1 μg ml^{-1}) and Nef for 24 h. n = 5. (h) NO was used to calculate the IC$_{50}$ of Nef. The concentrations were plotted on the x-axis in a linear fashion, and the inhibitory effect on NO was shown on the y-axis. n = 5. (i) BAP31 knockdown reversed Nef-mediated inhibition of LPS-induced TNF-α and iNOS mRNA expressions as determined by RT-PCR in BV2 cells. Cells were treated with LPS (1 μg ml^{-1}) and Nef (10 μM) for 6 h for TNF-α and iNOS mRNA detection. n = 5. *P < 0.05, significantly different from N.C. siRNA group; ns, no significant difference.

key proteins associated with inflammation. Notably, based on the effect of Nef on organelles in the cell painting analysis, BAP31 was identified as a promising cellular target of Nef for further study (Figure 2b,c). To verify BAP31 as a direct target of Nef, we expressed a GFP-tagged BAP31 protein in HEK293T cells and performed the MST experiment. Our result indicated that the dissociation constant (K_D) between Nef and BAP31 was 5.91 μM (Figures 2d and S1a). Additionally, the CETSA experiment demonstrated that Nef bound directly to BAP31 (Figure 2e). Considering the C-terminal cytoplasmic domain of BAP31 (amino acids 124–242) as a potential drug-binding region, we subsequently expressed this domain. The SPR experiment confirmed that Nef bound directly to the C-terminal cytoplasmic domain of BAP31, with the K_D value of 4.98 ± 1.80 μM (Figure 2f). To investigate the role of BAP31 in the anti-inflammatory capacity of Nef, small interfering RNA (siRNA) was employed to specifically silence BAP31 in BV2 cells (Figure S1b). The results indicated that the inhibitory effect of Nef on NO release was significantly diminished upon BAP31 knockdown, with an IC$_{50}$ value of 4.37 to 15.16 μM (Figure 2g,h). Meanwhile, Nef lost the inhibitory effect against LPS-induced TNF-α and iNOS after BAP31 knockdown (Figure 2i), further supporting the hypothesis that BAP31 serves as the cellular target to inhibit microglial activation.

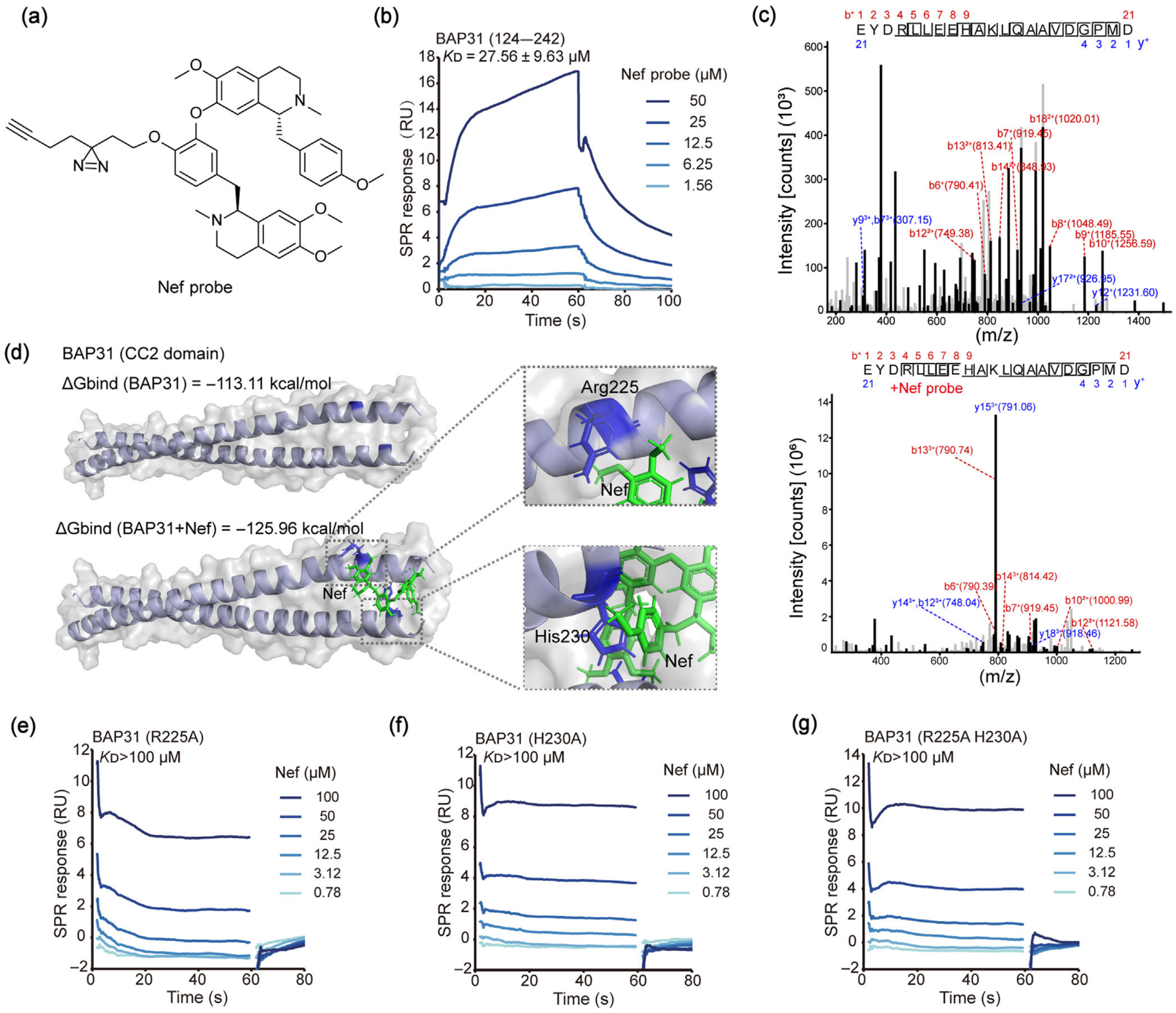

FIGURE 3 **Nef binds to the CC2 domain of BAP31 through electrostatic and pi–pi interactions.** (a) The chemical structure of Nef probe. (b) SPR assay of Nef probe with the truncated variant of BAP31 (amino acids 124–242). n = 5. (c) LC-MS/MS identification of BAP31 (amino acids 124–242) specific peptide segment modified by Nef probe. (d) Molecular docking and molecular dynamics simulation of Nef to the truncated variant of BAP31 (amino acids 124–242). (e–g) SPR assay of Nef with the truncated variant of BAP31 (amino acids 124–242). (e) Mutation of Arg residue at position 225 to Ala in the truncated variant of BAP31 (amino acids 124–242). (f) Mutation of His residue at position 230 to Ala in the truncated variant of BAP31 (amino acids 124–242). (g) Mutation of Arg at position 225 and His at position 230 to Ala in the truncated variant of BAP31 (amino acids 124–242).

3.3 | Nef binds to the CC2 domain of BAP31 through electrostatic and pi–pi interactions

We then investigated how Nef interacted with BAP31. We synthesised the Nef probe by introducing a difunctional chain with a diazirine and an alkyne to identify the binding sites between Nef and BAP31 (Figure 3a). The probe-related spectral data were presented in Figures S2–S4. The SPR experiment revealed that the K_D between the Nef probe and BAP31 (amino acids 124–242) was 27.56 ± 9.63 μM (Figure 3b), indicating a direct binding ability. Subsequently, the Nef probe was incubated with the recombinant BAP31 protein (amino acids 124–242) and crosslinked by ultraviolet irradiation for LC-MS/MS analysis. The results indicated that peptide segment 223–242 was the primary site for the Nef-probe modification (Figure 3c). To further investigate the binding mode of Nef with BAP31, we employed molecular docking to explore potential binding groups and the chemical bonds (Figure 3d). The results demonstrated that both electrostatic and pi–pi interactions significantly contributed to the binding of Nef with BAP31. Therefore, we postulated that Nef bound to two BAP31 proteins, thereby facilitating the dimerisation progress. Specifically, Nef attached to the Arg225 residue of one BAP31, while the opposite end of Nef interacted with the His230 residue of a different BAP31.

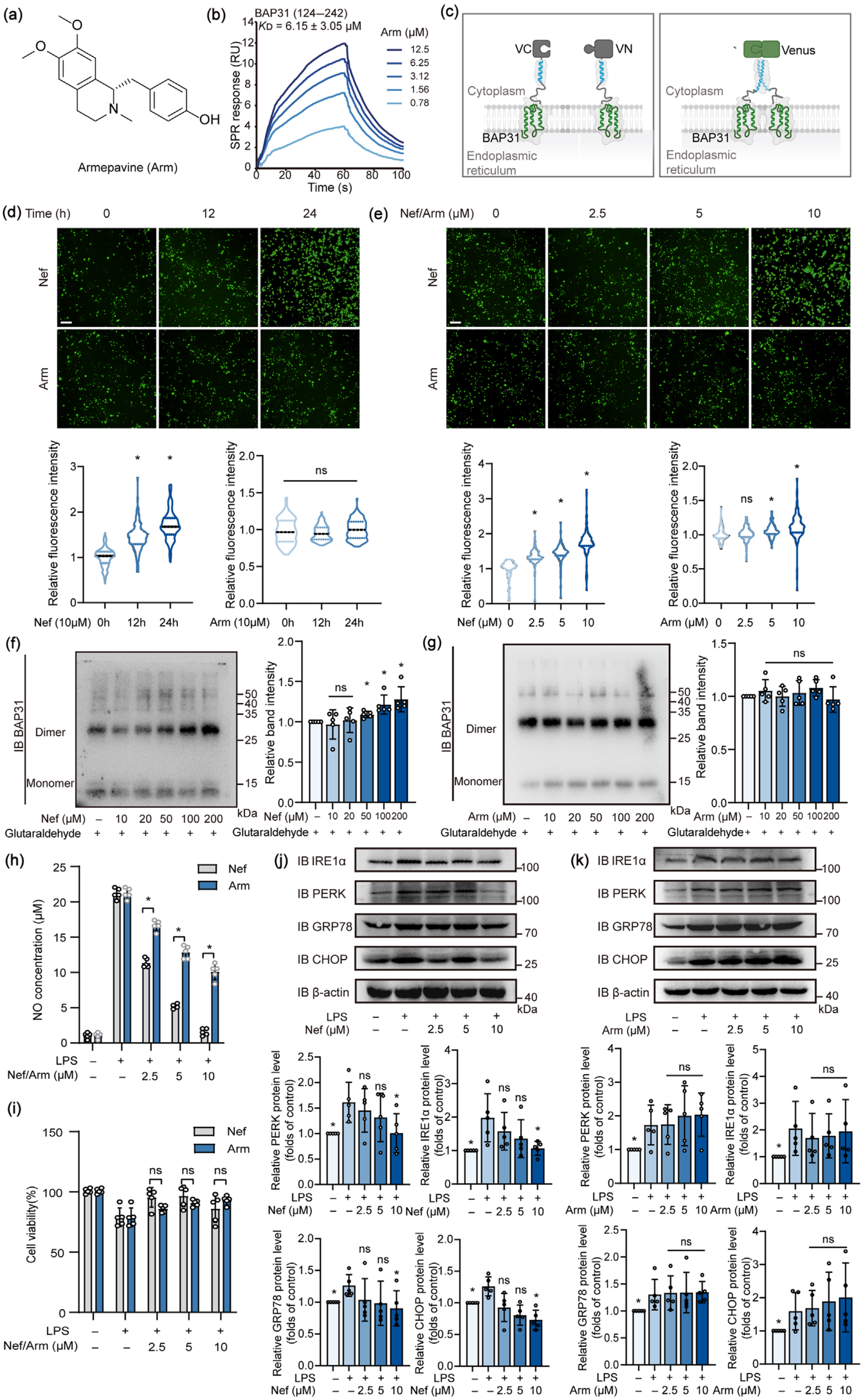

FIGURE 4 Legend on next page.

FIGURE 4 **Nef significantly induces the dimerisation process of BAP31.** (a) The chemical structure of Arm. (b) SPR assay of Arm with the BAP31 (amino acids 124–242). n = 5. (c) Schematic diagram of BiFC system for BAP31 dimerisation. (d) BiFC assay for BAP31 dimerisation at different time points. Cells were treated with Nef or Arm (10 μM) for 0, 12 and 24 h. Scale bar, 100 μm. (e) BiFC assay for BAP31 dimerisation with different concentrations. Cells were treated with Nef or Arm (2.5, 5 and 10 μM) for 24 h. scale bar, 100 μm. (f) Western blotting and quantification for the truncated BAP31 (amino acids 124–242) oligomerisation treated with Nef. The protein was incubated with Nef at room temperature for 2 h and crosslinked with 0.05% glutaraldehyde for 10 min. n = 5. (g) Western blotting and quantification for the truncated BAP31 (amino acids 124–242) oligomerisation treated with Arm. The protein was incubated with Arm for 2 h and crosslinked with 0.05% glutaraldehyde for 10 min. n = 5. (h) Nef inhibited the release of NO, whereas Arm did not possess this ability. Cells were treated with LPS (1 μg ml^{-1}) and Nef (2.5, 5 and 10 μM) for 24 h. n = 5. (i) MTT assay for cell viability after Nef and Arm treatment. Cells were treated with LPS (1 μg ml^{-1}), Nef (2.5, 5 and 10 μM) and Arm (2.5, 5 and 10 μM) for 24 h. n = 5. (j,k) Nef inhibited LPS-induced ER stress, whereas Arm did not exhibit such inhibitory effect. (j) Cells were treated with LPS (1 μg ml^{-1}) and Nef (2.5, 5 and 10 μM) for 3 h. (k) Cells were treated with LPS (1 μg ml^{-1}) and Arm (2.5, 5 and 10 μM) for 3 h. n = 5. $^*P < 0.05$, significantly different from model group; ns, no significant difference.

To further characterise the stabilisation effect, we performed molecular dynamics simulations to calculate the binding free energy of both the BAP31 dimer and the Nef-BAP31 complex. Thermodynamic quantification revealed that the binding free energy (ΔG) of the isolated BAP31 dimer was −113.11 kcal mol^{-1}, whereas the Nef-BAP31 complex exhibited a significantly reduced ΔG value of −125.96 kcal mol^{-1}. This significant reduction in energy thermodynamically confirmed that the binding of Nef substantially enhanced the structural stability of the BAP31 dimer. We next conducted SPR to explore whether mutations at the Arg225 and His230 sites resulted in an impact on the binding between Nef and BAP31. As shown in Figure 3e–g, the R225A and H230A mutations obviously reversed the binding of Nef with BAP31. Therefore, these results suggest that Nef primarily binds to Arg225 and His230 of BAP31 though a specific electrostatic and pi–pi interactions.

3.4 | Nef significantly induces the dimerisation process of BAP31 in LPS-induced BV2 cells

Based on the results of molecular docking, we proposed that Nef promoted the dimerisation of BAP31. In fact, Nef possesses a symmetrical topological molecular structure composed of two analogous fragments. The chemical structure of Nef can be characterised as a dimer composed of two fragments similar to armepavine (Arm) (Figure 4a). The SPR experiment ($K_D = 6.15 \pm 3.05$ μM) indicated that the dissociation constant between Arm and BAP31 (amino acids 124–242) was similar to Nef (Figure 4b), indicating a high similarity in the binding affinities to BAP31. We hypothesised that Nef facilitated BAP31 interaction through a mechanism akin to ‘molecular glue’. ‘Molecular glue’ refers to a small molecule that modulates protein–protein interactions by enhancing binding affinity between proteins, thereby facilitating novel protein interactions or stabilising pre-existing ones (Dewey et al., 2023). Subsequently, we constructed a BiFC reporter system to confirm the dimerisation of the BAP31. The dimerisation of proteins induced the formation of a complete green fluorescent protein (Venus), which emitted green fluorescence for detection (Figure 4c). During the treatment with Nef or Arm, Nef significantly promoted the continuous increase in green fluorescence intensity, suggesting the potent promotion of the BAP31 dimerisation. In contrast, Arm did not enhance the green fluorescence during this process (Figure 4d). Subsequent concentration-dependent experiments revealed that Nef significantly enhanced the green fluorescence intensity, whereas Arm did not exhibit a similar effect (Figure 4e). Moreover, we conducted chemical crosslinking experiments to further investigate the effect of the Nef on the dimerisation of BAP31. Our results indicated that upon the treatment of the glutaraldehyde as a crosslinking agent, Nef, but not Arm, significantly induced the dimerisation process of the recombinant protein BAP31 (amino acids 124–242) (Figure 4f,g). We attempted to explore the role of BAP31 dimerisation in microglial activation. We found that the inhibitory effect of Arm on NO production was markedly weaker than that of Nef (Figure 4h). Moreover, neither of the two compounds caused an obvious cytotoxic effect (Figure 4i). Considering that BAP31 is a typical ER-localised protein, we further investigated the effect of Nef on the expression of ER stress-related markers. Our results indicated that Nef effectively inhibited the expression of ER stress-related proteins, including IRE1α, PERK, GRP78 and CHOP (Figure 4j). However, Arm did not show effects similar to Nef (Figure 4k), suggesting that Nef might promote the BAP31 dimerisation to potentially maintain ER homeostasis during microglial activation. Therefore, these results indicate that Nef effectively promotes BAP31 dimerisation through the unique ‘molecular glue’-like mechanism in activated microglia.

3.5 | Nef inhibits the ER-mitochondria interaction to maintain energy homeostasis in LPS-induced BV2 cells

As shown in Figure 5a, flow cytometric analysis exhibited a significant elevation of MitoSOX fluorescence in LPS groups, which was effectively blocked by Nef treatment. Meanwhile, STED images stained with PKMITO indicated that LPS induced the marked alterations in mitochondrial morphology. We then performed quantitative measurements on the STED images (Figure 5b), objectively comparing mitochondrial morphology by statistically analysing circularity, area and perimeter. These analyses demonstrated that in normal cells, Nef treatment reduced circularity, indicating alleviation of LPS-induced mitochondrial swelling, whereas increased area and perimeter

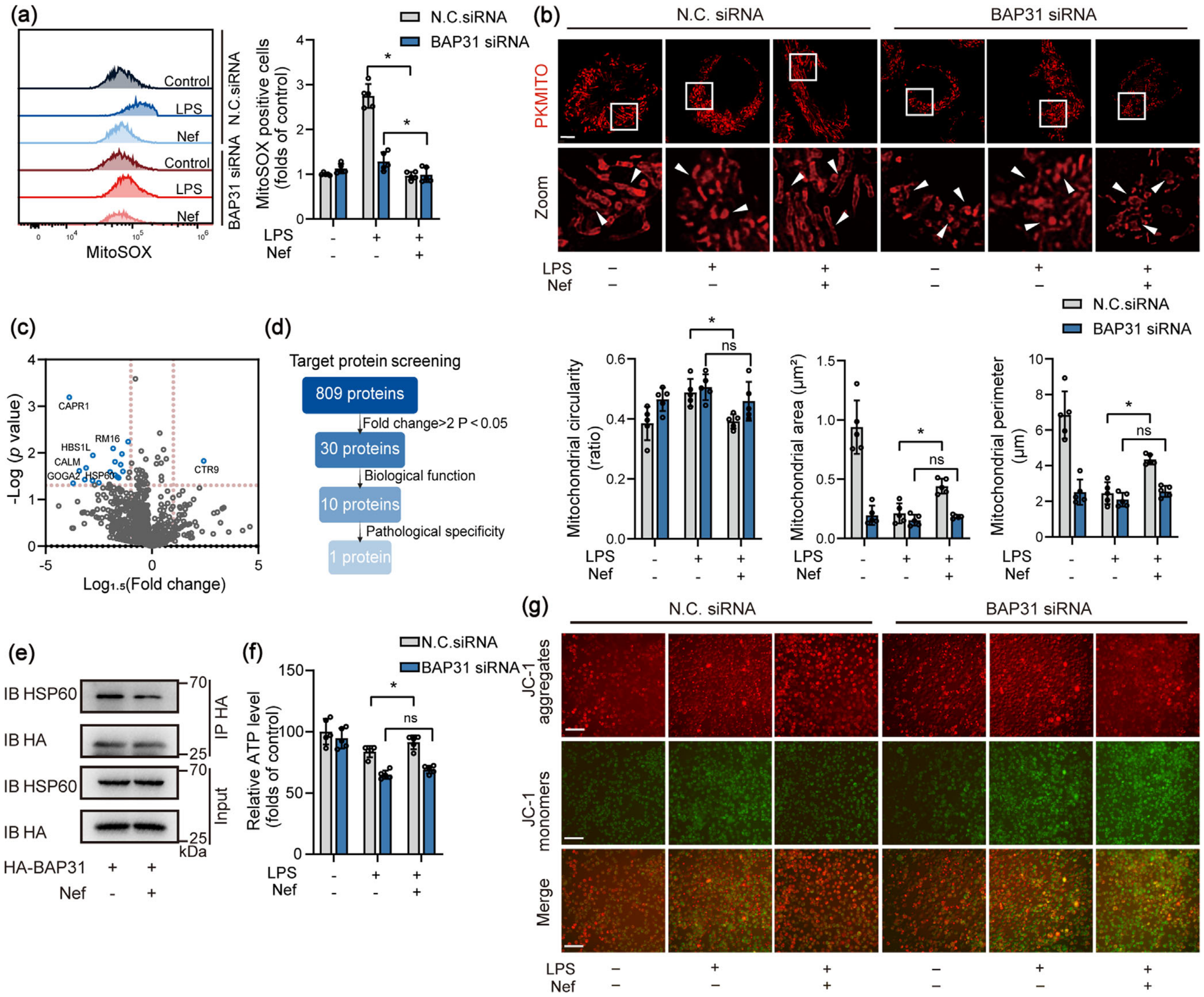

FIGURE 5 **Nef inhibits the ER-mitochondria interaction to maintain energy homeostasis in LPS-induced BV2 cells.** (a) Flow cytometric analysis of microglia for mtROS. Cells were treated with LPS (1 μg ml^{-1}) and Nef (10 μM) for 24 h. n = 5. (b) STED image of mitochondrial morphology in BV2. Cells were treated with LPS (1 μg ml^{-1}) and Nef (10 μM) for 6 h. Scale bar, 10 μm. Statistics were conducted on the circularity, area and perimeter of mitochondria. (c) Volcano plot for identifying the interacting proteins of BAP31 using APEX2. (d) Schematic diagram of the BAP31-binding proteins identification process. (e) Co-IP assay of the interaction between BAP31 and HSP60. n = 5. (f) ATP level analysis in BV2. Cells were treated with LPS (1 μg ml^{-1}) and Nef (10 μM) for 24 h. n = 5. (g) JC-1 staining of BV2 to assess mitochondrial membrane potential. Cells were treated with LPS (1 μg ml^{-1}) and Nef (10 μM) for 24 h. Scale bar, 50 μm. *$P < 0.05$, significantly different from N.C. siRNA group; ns, no significant difference.

reflected mitigation of mitochondrial fragmentation. Of note, in BAP31 knockdown cells, Nef failed to reverse LPS-induced damage. Thus, these observations suggest that Nef fundamentally modulates the ER stress, thereby enhancing mitochondrial function.

Next, we aimed to explore the potential mechanisms underlying the BAP31-mediated interactions between the ER and mitochondria. Here, we utilised the APEX2 proximity labelling system to conduct a large-scale screening of the interacting proteins of BAP31. Then, we detected a total of 809 BAP31-binding proteins through mass spectrometry (Figure 5c). Among these, we mainly focused on the proteins that exhibited a reduced binding affinity for BAP31 after Nef treatment, thereby revealing the interaction mechanism between the ER and mitochondria. Notably, the heat shock protein 60 (HSP60) has garnered particular attention (Figure 5d) due to its vital role as a molecular chaperone in mitochondria for maintaining ATP-producing function (Gazali, 2012). HSP60 also plays a fundamental role in facilitating the proper folding, assembly, transport and degradation of proteins in mitochondria (Radford, 2006). Next, co-IP experiment confirmed that Nef significantly inhibited the BAP31–HSP60 interaction (Figure 5e). Notably, we found that Nef significantly inhibited the decrease in mitochondrial membrane potential and promoted the production of ATP (Figure 5f,g). Meanwhile, these observations were

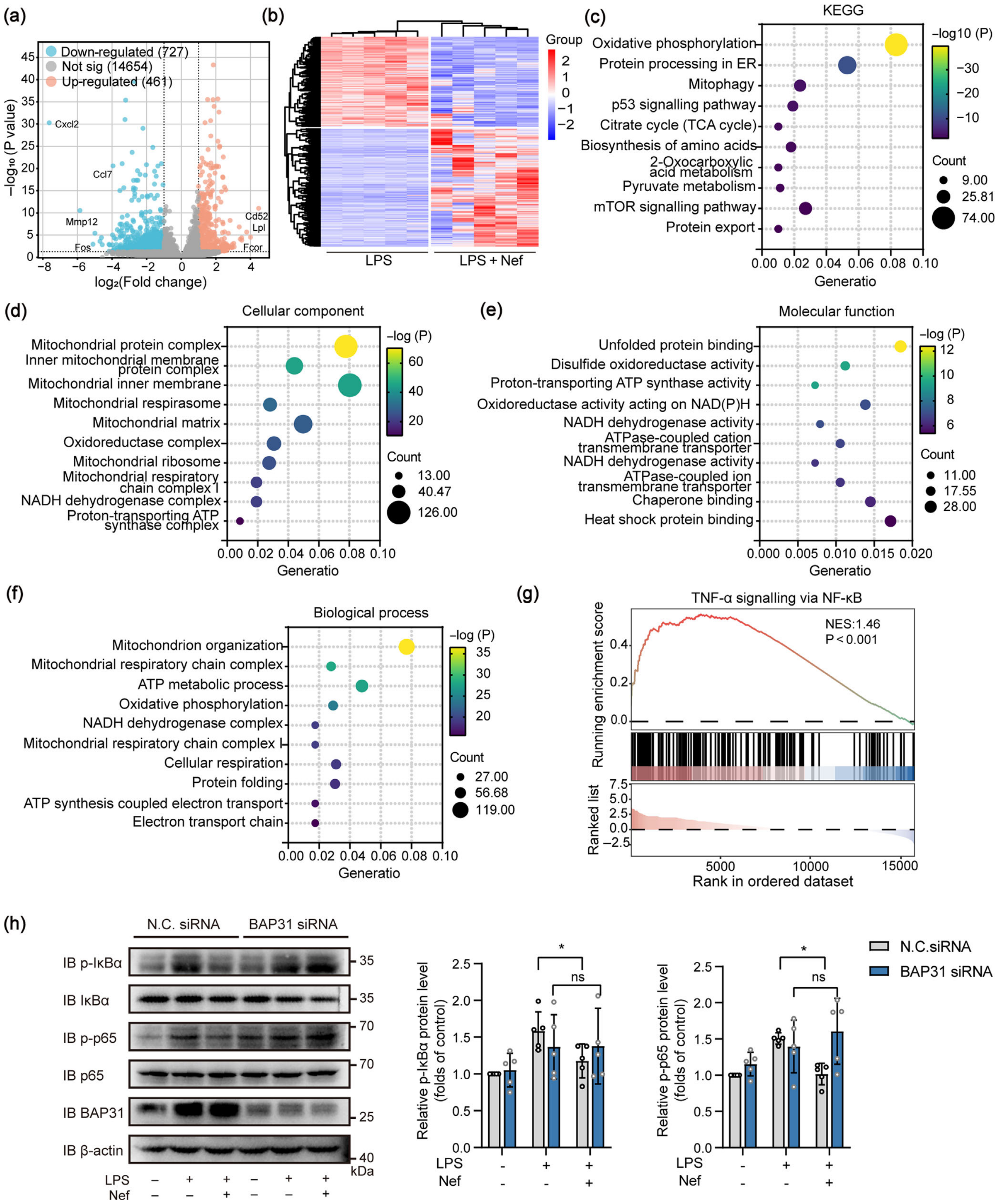

FIGURE 6 Legend on next page.

FIGURE 6 **Nef modulates mitochondrial energy metabolism through ER–mitochondria crosstalk.** (a) Volcano plot of gene expressions in BV2 cells treated with LPS in the presence of Nef. Cells were treated with LPS (1 μg ml^{-1}) and Nef (10 μM) for 24 h. n = 5. (b) Heatmap of cluster analysis for LPS (1 μg ml^{-1}) treatment and Nef (10 μM) treatment. (c) KEGG pathway analysis revealed differential gene expression signatures, as illustrated by the bubble chart. (d–f) Bubble plot displays gene expression variations mapped to cellular component, molecular function and biological process through enrichment analysis. (g) Gene set enrichment analysis (GSEA) verified the gene expression changes to TNF-α signalling pathway after Nef treatment. (h) BAP31 knockdown reversed Nef-mediated inhibition of LPS-induced TNF-α signalling pathway. Cells were treated with LPS (1 μg ml^{-1}) and Nef (10 μM) for 1 h. n = 5. *$P < 0.05$, significantly different from N.C. siRNA group; ns, no significant difference.

significantly reversed upon BAP31 knockdown (Figure 5f,g). Therefore, we speculate that the binding of BAP31 to HSP60 may facilitate the interaction between the ER and mitochondria, thereby enhancing the energy homeostasis of mitochondria during microglial activation.

3.6 | Nef modulates mitochondrial energy metabolism through ER-mitochondria crosstalk in LPS-induced BV2 cells

To further explore the downstream signalling pathways of ER–mitochondria crosstalk, we conducted the RNA sequencing assay. In the volcano plot and clustering heatmap, a total of 461 genes were down-regulated, and 727 genes were up-regulated (Figure 6a,b). This observation indicated that Nef treatment led to significant alterations in the expression levels of a subset of genes. Moreover, the Kyoto Encyclopedia of Genes and Genomes (KEGG) pathway enrichment analysis revealed that Nef treatment significantly impacted ER protein processing and mitochondrial-associated pathways including oxidative phosphorylation, mitophagy and the citrate cycle (Figure 6c). Notably, Gene Ontology (GO) analysis was conducted, and the results were presented in bubble plots (Figure 6d–f). The results demonstrated specific enrichment in cellular components related to the inner mitochondrial membrane protein complex, mitochondrial respiratory chain complex I and proton-transporting ATP synthase complex (Figure 6d). Molecular functions were prominently associated with NADH dehydrogenase activity and ATPase-coupled ion transmembrane transporter activity (Figure 6e), suggesting that Nef may influence energy metabolism through modulation of mitochondrial electron transport chain functionality. Further investigations revealed that Nef administration markedly affected core mitochondrial processes including mitochondrial respiratory chain complex assembly and ATP metabolic process, indicating multi-level regulation of mitochondrial energy metabolism. Concurrent enrichment of ER-related functions such as unfolded protein binding and chaperone binding implied potential regulatory effects of Nef on mitochondrial homeostasis through modulation of ER–mitochondria interactions (Figure 6f). Based on gene set enrichment (GSEA) analysis, we found that the TNF-α signalling pathway was highly involved in the activation of microglia (Figure 6g). Therefore, we subsequently conducted western blotting to confirm the activation of these pathways. As shown in Figure 6h, Nef decreased phosphorylation levels of IκB-α and p65. Crucially, the inhibitory effect of Nef on NF-κB pathway activation was substantially attenuated upon BAP31 knockdown, demonstrating that BAP31 mediates Nef-dependent regulatory effect on mitochondrial function and inflammatory signal transduction.

3.7 | Nef inhibits the microglial activation in the LPS-induced mouse inflammation model

We constructed an LPS-induced neuroinflammation mouse model to further explore the role of Nef in neuroinflammation. The 10 and 50 mg kg^{-1} doses of Nef were selected for evaluating its anti-neuroinflammatory and neuroprotective effects based on well-established efficacy in prior murine models: 10 mg kg^{-1} demonstrated therapeutic benefits in pulmonary fibrosis, liver ischaemia–reperfusion and cerebral ischaemia, while 50 mg kg^{-1} showed effectiveness in anti-diabetic, kidney injury and AD models. The experimental procedure was illustrated in Figure 7a. Mice received pre-treatment for 3 days prior to LPS administration, and subsequent analysis was conducted 24 h later. First, we evaluated the serum levels of TNF-α and IL-1β. As shown in Figure 7b,c, our findings indicate that LPS treatment significantly elevated the serum levels of TNF-α and IL-1β; however, Nef treatment effectively reduced these levels. Immunohistochemistry (IHC) staining for Iba-1 and TNF-α was used to evaluate microglial activation in brain tissue and the therapeutic effect of Nef. As shown in Figure 7d, Iba-1-positive microglia exhibited larger somas and increased branching following LPS injections; conversely, Nef significantly attenuated microglial activation, as indicated by the decrease in Iba-1-positive cells (Figure 7e). Meanwhile, TNF-α staining revealed an increased expression in LPS-treated brain tissue, which was subsequently reduced following Nef treatment (Figure 7f). Notably, CHOP serves as a biomarker of ER stress. Immunohistochemistry analysis revealed a significant increase in CHOP-positive cells within the LPS-treated group, which was markedly attenuated following Nef intervention (Figure 7g). These findings suggest that Nef suppresses the unfolded protein response (UPR) and mitigates ER stress-associated cellular dysfunction. Furthermore, immunohistochemical evaluation of 8-hydroxy-2′-deoxyguanosine (8-OHdG), a specific biomarker for DNA oxidative damage, demonstrated enhanced accumulation of 8-OHdG-positive cells in LPS-treated groups. Importantly, treatment with Nef effectively reduced 8-OHdG-positive cell counts (Figure 7h). This evidence indicates that Nef alleviates microglia-mediated oxidative stress by diminishing LPS-induced ROS generation. Nissl staining was employed to characterise the morphological damage to neurons in brain tissue. As shown in Figure 7i, LPS-induced neurons displayed irregular shapes and signs of

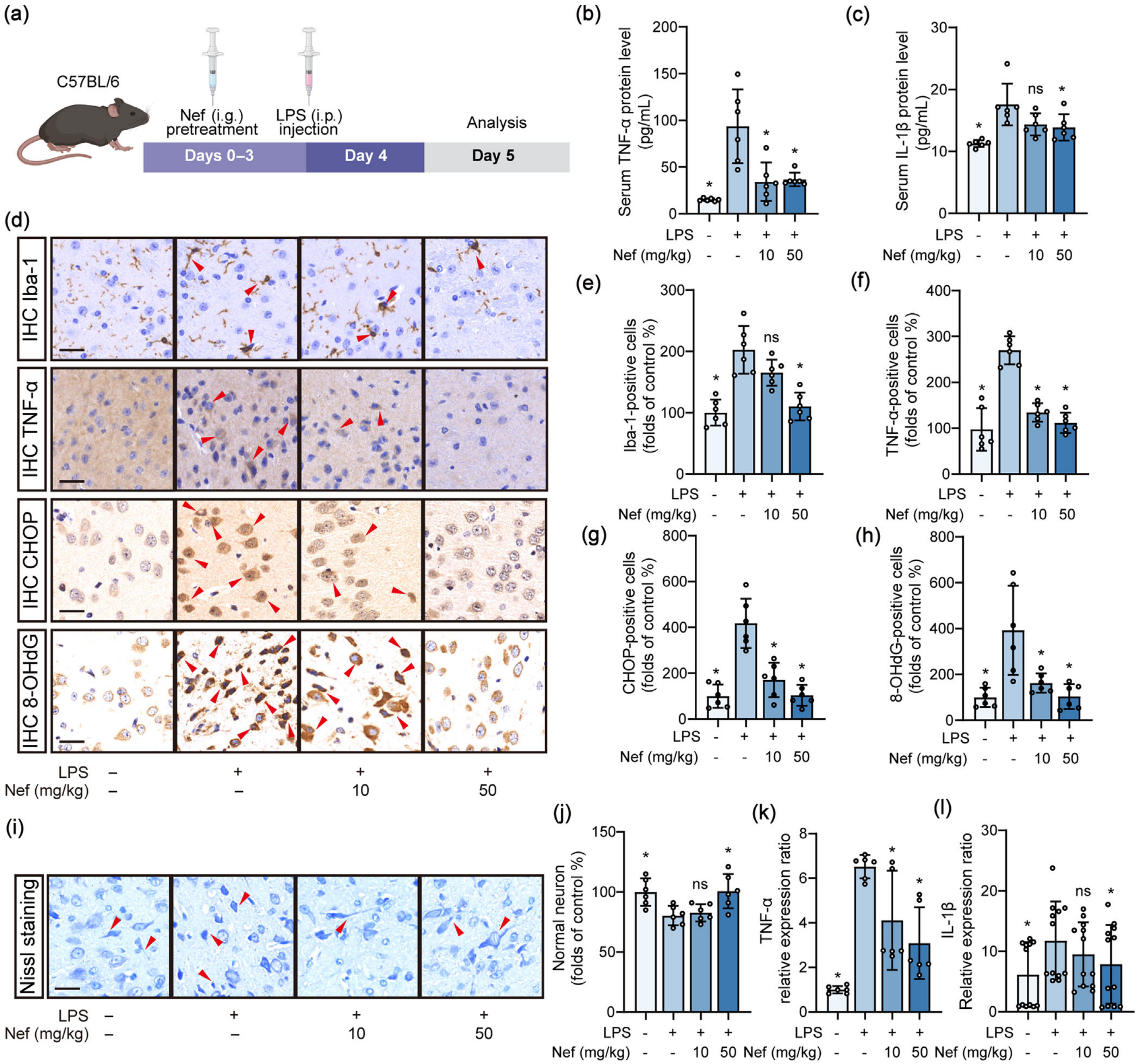

FIGURE 7 **Nef inhibits the microglial activation in the LPS-induced mouse inflammation model.** (a) Schedule of animal treatments. (b,c) Detection of TNF-α and IL-1β in animal serum by ELISA. n = 6. (d) Immunohistochemistry (IHC) staining for Iba-1, TNF-α, CHOP and 8-OHdG of the cortex in mice. Arrowheads indicate the Iba-1, TNF-α, CHOP and 8-OHdG-positive cells. Scale bar, 25 μm. (e–h) Quantitative analysis of Iba-1, TNF-α, IHC, CHOP and 8-OHdG IHC staining of mice. n = 6. (i) Nissl staining of the cortex in mice. Arrowheads indicate the normal neurons. Scale bar, 25 μm. (j) Quantitative analysis of Nissl staining of mice. n = 6. (k, l) Nef inhibited LPS-induced TNF-α and IL-1β mRNA expression by RT-PCR. n = 6. Percent of positive cells was calculated by ImageJ. For an unbiased analysis, six photomicrographs were measured in the positive cell analysis (fold of control %). *$P < 0.05$, significantly different from model group; ns, no significant difference.

shrinkage. However, Nef significantly reduced the degree of Nissl body disruption, bringing the neurons closer to normal morphology (Figure 7j). We further examined the gene expression of different inflammatory mediators in brain tissue, including TNF-α and IL-1β. As shown in Figure 7k,l, LPS significantly up-regulated the mRNA levels of TNF-α and IL-1β. However, treatment with Nef significantly reversed the expression of TNF-α and IL-1β. Taken together, these findings collectively indicate that Nef exerts a protective effect against neuroinflammation and neuronal damage induced by LPS.

3.8 | Nef protects neuronal damage by inhibiting microglial activation in the MCAO mouse model

To gain insights into the role of Nef in cerebral ischaemic injury, we examined the effects in the mouse model of MCAO. The experimental schedule is shown in Figure 8a. The TTC-stained brain sections clearly revealed the infarct regions, and the assessment of infarct volume was shown in Figure 8b. Our findings indicate that MCAO significantly increased the infarct volume, which was substantially reversed

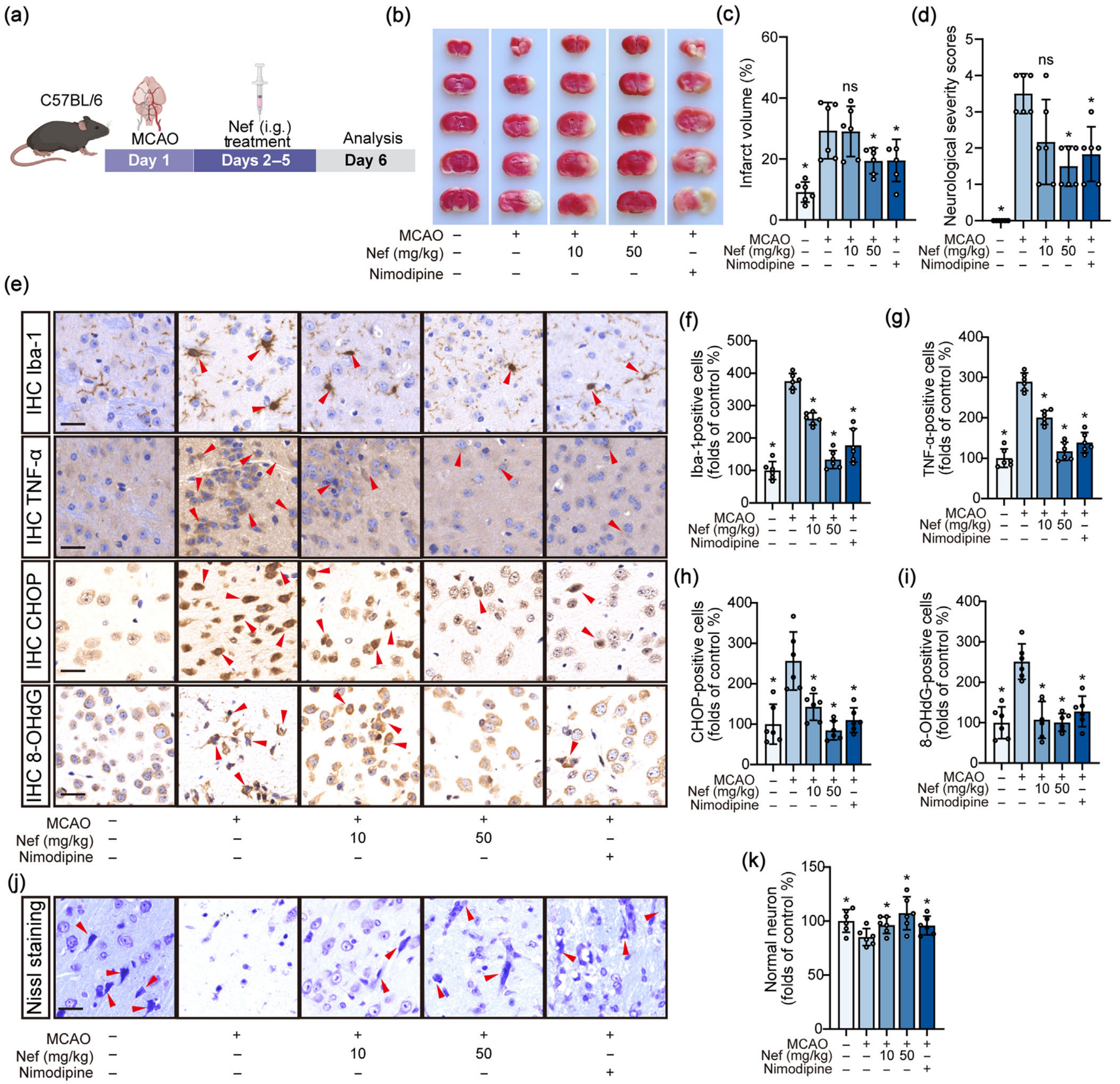

FIGURE 8 **Nef protects neuronal damage by inhibiting microglial activation in MCAO mouse model**. (a) Schedule of animal treatments. (b) Representative photographs of TTC-stained coronal sections. (c) Nef reduced ischaemic volume induced by MCAO. n = 6. (d) Nef decreased MCAO-induced mice neurological deficits. (e) Immunohistochemistry (IHC) staining for Iba-1, TNF-α, CHOP and 8-OHdG of the cortex in mice. Arrowheads indicate the Iba-1, TNF-α, CHOP and 8-OHdG-positive cells. Scale bar, 25 μm. (f–i) Quantitative analysis of Iba-1, TNF-α, IHC, CHOP and 8-OHdG IHC staining of mice. n = 6. (j) Nissl staining of the cortex in mice. Arrowheads indicate the normal neurons. Scale bar, 25 μm. (k) Quantitative analysis of Nissl staining of mice. n = 6. Percent of positive cells was calculated by ImageJ. For an unbiased analysis, six photomicrographs were measured in the positive cell analysis (fold of control %). *$P < 0.05$, significantly different from model group; ns, no significant difference.

by Nef treatment (Figure 8c). Moreover, the evaluation of neurological severity scores showed that MCAO group had a higher score, suggesting more severe neurological deficits. However, Nef showed a significant reduction in the score (Figure 8d). Thus, these findings suggested that Nef treatment effectively alleviated the neurological deficits induced by MCAO.

In the immunohistochemical staining for Iba-1 in the MCAO group, the microglia exhibited a significant up-regulation of Iba-1 expression and underwent a notable increase with branches. However, Nef exhibited a significant reduction in microglial activation, as evidenced by the decreased number of Iba-1-positive cells (Figure 8e,f). Moreover, a notable increase in the expression of TNF-α was observed in the MCAO group. In contrast, the group treated with Nef exhibited a significant reduction in both the number of TNF-α-positive cells and the intensity of staining (Figure 8e,g). These results indicated that Nef effectively suppressed the expression of TNF-α in the context of MCAO. Furthermore, immunohistochemical analysis of CHOP revealed that Nef significantly reversed the MCAO-induced elevation of CHOP levels (Figure 8e). Quantitative evaluation demonstrated a marked reduction in CHOP-positive cell counts following Nef administration (Figure 8h), indicating that Nef mitigates downstream inflammatory responses by suppressing ER stress triggered by MCAO. Furthermore, immunohistochemical assessment of 8-OHdG demonstrated that Nef treatment effectively reduced 8-OHdG accumulation in cerebral cells compared to the MCAO group (Figure 8e,i). This observation suggests that Nef substantially attenuates ROS-mediated injury induced by MCAO. In the Nissl staining, neurons exhibited morphological damage in the MCAO group. Of note, numerous neurons exhibited shrunken cell bodies, accompanied by a disruption and reduction in the density of Nissl bodies (Figure 8j). In the group treated with Nef, neurons showed a degree of morphological improvement suggesting that Nef protected neurons from MCAO-induced injury (Figure 8k). Collectively, these results suggest that Nef possesses a neuroprotective effect against cerebral ischaemia–reperfusion injury induced by MCAO, providing significant evidence supporting the potential therapeutic application of Nef for ischaemic stroke.

4 | DISCUSSION

Emerging evidence establishes BAP31 as an ER-resident hub coordinating microglial activation through inflammatory cascades. Mechanistically, BAP31 amplifies neuroinflammation by enhancing IRAK1-dependent pro-inflammatory cytokine release (Liu et al., 2019), activating NF-κB/c-Jun transcriptional networks linked to synaptic dysfunction (He et al., 2024; Li et al., 2023) and driving NADPH oxidase-mediated superoxide overproduction via p22phox–Keap1 redox signalling (Liu et al., 2021). These findings position BAP31 as a master regulator bridging immune activation and neuronal damage. Despite the potential therapeutic promise of BAP31 for neuroinflammatory disorders, no pharmacologically tractable BAP31 modulators have been reported. Thus, the discovery of lead drugs targeting BAP31 to decouple microglial hyperactivation is of significant importance for improving neuronal pathophysiology. Here, we identified the natural compound Nef as a BAP31 modulator that suppresses neuroinflammation via ER-mitochondria decoupling. Further analyses demonstrated unique symmetric topology of Nef enabled simultaneous binding to two BAP31 monomers, thereby driving homodimer formation. This steric reorganisation disrupted BAP31–HSP60 complexes at mitochondria–ER contact sites (MERCs), ultimately attenuating inflammatory mediator release and rescuing cerebral ischaemia outcomes. Of note, competitive binding assays with Arm as a structural analogue lacking symmetry revealed selective inhibition of Nef–BAP31 interaction without dimerisation capacity. Therefore, these observations highlight the dual functionality of Nef: (1) high-affinity BAP31 engagement and (2) symmetry-driven homodimer stabilisation. Unlike conventional ‘heterodimer glue’ scaffolds, the unique molecular topology of Nef provides a blueprint for homodimer-inducing agents as an underexplored therapeutic strategy.

The ER is the largest organelle in the cells and possesses an extensive network of tubules and cisternae. The ER interacts continuously with most other organelles, especially the mitochondria. Although previous studies have established that BAP31 is predominantly localised in the ER, our cell painting analyses indicated that Nef not only modulated the morphology of the ER but also induced significant alterations in the mitochondria, which greatly raised our interest. In fact, the interaction between the ER and mitochondria occurs at specialised membrane contact sites, MERCs (Marchi et al., 2014). These MERCs function as distinct cellular substructures, primarily serving as platforms for organelle interaction and cellular signal transduction. Notably, MERCs have been extensively reported to play a crucial role in calcium (Ca^{2+}) signalling, energy homeostasis, redox biology and inflammation (Csordas et al., 2010; Giacomello et al., 2010; Hamasaki et al., 2013; Hirota & Tanaka, 2009; Korobova et al., 2013; Rimessi et al., 2009). Moreover, current studies indicate that MERCs participate in the regulation of multiple signalling pathways, including inflammation and immune responses with various neurological diseases such as cerebral ischaemia, AD and PD (Hedskog et al., 2013). Hence, the pharmacological control of MERCs may counteract the self-amplifying inflammatory loops associated with microglial activation. Notably, our findings provide a conceptual validation for the development of small molecules that destabilize MERCs. Furthermore, the identification of Nef-dependent mechanisms targeting MERCs reveals new opportunities for the treatment of neuroinflammatory disorders, underscoring the significant translational potential.

The ER is regarded as the primary store of calcium in cells. BAP31 plays a significant role in maintaining calcium concentrations in the ER. Since mitochondria are not static and continuously undergo dynamic processes of fusion and fission, the dimerisation of BAP31 may alter the interaction between the ER and mitochondria by modulating the specific protein interactions between these two organelles. Here, our findings delineated a previously unrecognized mechanism through which Nef modulated organelle communication during inflammatory responses. Crucially, structural mapping analyses demonstrated that Nef specifically targeted the CC2 domain of BAP31, which was a critical ER-resident protein governing organelle tethering. In particular, the Nef–BAP31 interaction disrupted the formation of BAP31–HSP60 complexes at ER-mitochondria contact sites. The functional consequences of this dissociation were effectively corroborated through ROS tracking using MitoSOX. Thus, these data collectively support a model wherein Nef acts as a molecular wedge at organelle communication hubs, effectively regulating pathological ER-to-mitochondria signalling cascades during neuroinflammation.

Nef demonstrates rapid systemic distribution with predominant hepatic accumulation and dose-dependent retention in renal/pulmonary tissues. Metabolised primarily by **CYP2D6** / **CYP3A4**, Nef generates bioactive derivatives that elevate drug-interaction potential

(Huang et al., 2007). Despite moderate oral bioavailability (65%), its high lipophilicity facilitates extensive tissue penetration, raising potential risks of off-target effects (L. Zhao et al., 2010; Y. Zhao et al., 2012). For example, hERG channel blockade by Nef confers a concerning proarrhythmic risk, underscoring the need for cardiac safety assessment prior to clinical development (Dong et al., 2012). Moreover, the selected experimental models were strategically employed to evaluate distinct neuroinflammatory mechanisms: The LPS-induced model (PAMP-driven) acutely activates **TLR4** / NF-κB signalling, serving as a robust platform to assess infection-related neuroprotection (Yang et al., 2020); conversely, the MCAO model (DAMP-mediated) recapitulates ischaemic stroke pathophysiology, involving **NLRP3** inflammasome activation and neurovascular injury (DeLong et al., 2022; Lakhan et al., 2009). Although these models differ fundamentally in their triggers and temporal dynamics, their complementary use enhances translational relevance by systematically targeting divergent neuroinflammatory pathways.

In summary, we demonstrate that Nef functions as a pharmacological agent by directly targeting BAP31 through a ‘molecular glue’ mechanism that remodels the contact between the ER and mitochondria. Crucially, this structural reorganisation preserves mitochondrial energy homeostasis, thereby blocking microglial polarisation towards a pro-inflammatory phenotype, particularly for ischaemic stroke.

AUTHOR CONTRIBUTIONS

Y.-X. Zhu: Data curation (lead); formal analysis (equal); methodology (equal); visualization (equal); writing—original draft (lead). **Z. Yang:** Investigation (equal); methodology (equal). **L. Li:** Formal analysis (equal); investigation (equal); methodology (equal). **Z.-K. Chen:** Methodology (equal). **F.-F. Zhuo:** Conceptualization (equal); formal analysis (equal). **Y.-H. Wang:** Formal analysis (equal). **Z.-P. Liu:** Resources (equal); visualization (supporting). **B. Han:** Validation (equal). **W. Yu:** Investigation (equal). **P.-F. Tu:** Conceptualization (equal); investigation (equal); writing—review and editing (equal). **T.-T. Wei:** Methodology (equal); validation (equal); writing—review and editing (equal). **H. Wang:** Conceptualization (equal); validation (equal); writing—review and editing (equal). **K.-W. Zeng:** Conceptualization (lead); funding acquisition (lead); resources (lead); writing—review and editing (lead).

ACKNOWLEDGEMENTS

This work was financially supported by Jinan New 20 Policies for Higher Education Funding (202228048), National Natural Sciences Foundation of China (82325050, 82174008 and U23A20529), Beijing Municipal Natural Science Foundation-Key Research Project of the Daxing (L246029), Beijing Municipal Natural Science Foundation (7232273), Natural Science Foundation of Shandong Province (Joint Foundation for Innovation and Development) (ZR2022LZY021), the Special Fund for “Tian-Chi Talent Introduction Program” and the Special Fund for Taishan Scholars Project in Shandong Province (tstp20230633).

CONFLICT OF INTEREST STATEMENT

The authors declare no competing interests.

DATA AVAILABILITY STATEMENT

Data supporting the findings of this study are available from the corresponding author upon request. Some data may not be made available due to privacy or ethical restrictions.

DECLARATION OF TRANSPARENCY AND SCIENTIFIC RIGOUR

This declaration acknowledges that this paper adheres to the principles for transparent reporting and scientific rigour of preclinical research as stated in the BJP guidelines for Natural Products Research, Design and Analysis, Immunoblotting and Immunochemistry, and Animal Experimentation and as recommended by funding agencies, publishers and other organizations engaged with supporting research.

ORCID

Hua Wang https://orcid.org/0000-0002-2605-5697

REFERENCES

Abe, F., Van Prooyen, N., Ladasky, J. J., & Edidin, M. (2009). Interaction of Bap31 and MHC class I molecules and their traffic out of the endoplasmic reticulum. *Journal of Immunology*, *182*(8), 4776–4783. https://doi.org/10.4049/jimmunol.0800242

Alexander, S. P. H., Kelly, E., Mathie, A., Peters, J. A., Veale, E. L., Armstrong, J. F., Faccenda, E., Harding, S. D., Pawson, A. J., Southan, C., Buneman, O. P., Cidlowski, J. A., Christopoulos, A., Davenport, A. P., Fabbro, D., Spedding, M., Striessnig, J., Davies, J. A., Ahlers-Dannen, K. E., … Zolghadri, Y. (2021). THE CONCISE GUIDE TO PHARMACOLOGY 2021/22: Introduction and other protein targets. *British Journal of Pharmacology*, *178*(Suppl 1), S1–S26. https://doi.org/10.1111/bph.15537

Alexander, S. P. H., Roberts, R. E., Broughton, B. R. S., Sobey, C. G., George, C. H., Stanford, S. C., Cirino, G., Docherty, J. R., Giembycz, M. A., Hoyer, D., Insel, P. A., Izzo, A. A., Ji, Y., MacEwan, D. J., Mangum, J., Wonnacott, S., & Ahluwalia, A. (2018). Goals and practicalities of immunoblotting and immunohistochemistry: A guide for submission to the British Journal of Pharmacology. *British Journal of Pharmacology*, *175*(3), 407–411. https://doi.org/10.1111/bph.14112

Annaert, W. G., Becker, B., Kistner, U., Reth, M., & Jahn, R. (1997). Export of cellubrevin from the endoplasmic reticulum is controlled by BAP31. *Journal of Cell Biology*, *139*(6), 1397–1410. https://doi.org/10.1083/jcb.139.6.1397

Breckenridge, D. G., Nguyen, M., Kuppig, S., Reth, M., & Shore, G. C. (2002). The procaspase-8 isoform, procaspase-8L, recruited to the BAP31 complex at the endoplasmic reticulum. *Proceedings of the National Academy of Sciences of the United States of America*, *99*(7), 4331–4336. https://doi.org/10.1073/pnas.072088099

Breckenridge, D. G., Stojanovic, M., Marcellus, R. C., & Shore, G. C. (2003). Caspase cleavage product of BAP31 induces mitochondrial fission through endoplasmic reticulum calcium signals, enhancing cytochrome c release to the cytosol. *Journal of Cell Biology*, *160*(7), 1115–1127. https://doi.org/10.1083/jcb.200212059

Chandra, D., Choy, G., Deng, X. D., Bhatia, B., Daniel, P., & Tang, D. G. (2004). Association of active caspase 8 with the mitochondrial membrane during apoptosis: Potential roles in cleaving BAP31 and caspase 3 and mediating mitochondrion-endoplasmic reticulum cross talk in etoposide-induced cell death. *Molecular and Cellular Biology*, *24*(15), 6592–6607. https://doi.org/10.1128/mcb.24.15.6592-6607.2004

Cho, I.-T., Adelmant, G., Lim, Y., Marto, J. A., Cho, G., & Golden, J. A. (2017). Ascorbate peroxidase proximity labeling coupled with biochemical fractionation identifies promoters of endoplasmic reticulum-mitochondrial contacts. *Journal of Biological Chemistry*, *292*(39), 16382–16392. https://doi.org/10.1074/jbc.M117.795286

Csordas, G., Varnai, P., Golenar, T., Roy, S., Purkins, G., Schneider, T. G., Balla, T., & Hajnoczky, G. (2010). Imaging interorganelle contacts and local calcium dynamics at the ER-mitochondrial interface. *Molecular Cell*, *39*(1), 121–132. https://doi.org/10.1016/j.molcel.2010.06.029

Curtis, M. J., Alexander, S. P. H., Cortese-Krott, M., Kendall, D. A., Martemyanov, K. A., Mauro, C., Panettieri, R. A. Jr., Papapetropoulos, A., Patel, H. H., Santo, E. E., Schulz, R., Stefanska, B., Stephens, G. J., Teixeira, M. M., Vergnolle, N., Wang, X., & Ferdinandy, P. (2025). Guidance on the planning and reporting of experimental design and analysis. *British Journal of Pharmacology*, *182*(7), 1413–1415. https://doi.org/10.1111/bph.17441

DeLong, J. H., Ohashi, S. N., O'Connor, K. C., & Sansing, L. H. (2022). Inflammatory responses after ischemic stroke. *Seminars in Immunopathology*, *44*(5), 625–648. https://doi.org/10.1007/s00281-022-00943-7

Dewey, J. A., Delalande, C., Azizi, S. A., Lu, V., Antonopoulos, D., & Babnigg, G. (2023). Molecular glue discovery: Current and future approaches. *Journal of Medicinal Chemistry*, *66*(14), 9278–9296. https://doi.org/10.1021/acs.jmedchem.3c00449

Dong, Z. X., Zhao, X., Gu, D. F., Shi, Y. Q., Zhang, J., Hu, X. X., Hu, M. Q., Yang, B. F., & Li, B. X. (2012). Comparative effects of liensinine and neferine on the human ether-a-go-go-related gene potassium channel and pharmacological activity analysis. *Cellular Physiology and Biochemistry*, *29*(3–4), 431–442. https://doi.org/10.1159/000338497

du Sert, N. P., Hurst, V., Ahluwalia, A., Alam, S., Avey, M. T., Baker, M., Browne, W. J., Clark, A., Cuthill, I. C., Dirnagl, U., Emerson, M., Garner, P., Holgate, S. T., Howells, D. W., Karp, N. A., Lazic, S. E., Lidster, K., MacCallum, C. J., Macleod, M., … Würbel, H. (2020). The ARRIVE guidelines 2.0: Updated guidelines for reporting animal research. *PLoS Biology*, *18*(7), e3000410. https://doi.org/10.1371/journal.pbio.3000410

Gazali, A. (2012). Taking the heat out of chaperokine function. *Immunotherapy*, *4*(8), 773–775. https://doi.org/10.2217/imt.12.78

Giacomello, M., Drago, I., Bortolozzi, M., Scorzeto, M., Gianelle, A., Pizzo, P., & Pozzan, T. (2010). Ca^{2+} hot spots on the mitochondrial surface are generated by Ca^{2+} mobilization from stores, but not by activation of store-operated Ca^{2+} channels. *Molecular Cell*, *38*(2), 280–290. https://doi.org/10.1016/j.molcel.2010.04.003

Hamasaki, M., Furuta, N., Matsuda, A., Nezu, A., Yamamoto, A., Fujita, N., Oomori, H., Noda, T., Haraguchi, T., Hiraoka, Y., Amano, A., & Yoshimori, T. (2013). Autophagosomes form at ER-mitochondria contact sites. *Nature*, *495*(7441), 389–393. https://doi.org/10.1038/nature11910

Hayashi, T., & Su, T.-P. (2007). Sigma-1 receptor chaperones at the ER-mitochondrion interface regulate Ca^{2+} signaling and cell survival. *Cell*, *131*(3), 596–610. https://doi.org/10.1016/j.cell.2007.08.036

He, J., Jin, D., Zhao, S., & Duan, M. (2024). BAP31 promotes adhesion between endothelial cells and macrophages through the NF-κB signaling pathway in sepsis. *Journal of Inflammation Research*, *17*, 1267–1279. https://doi.org/10.2147/jir.S448091

Heath-Engel, H. M., Wang, B., & Shore, G. C. (2012). Bcl2 at the endoplasmic reticulum protects against a Bax/Bak-independent paraptosis-like cell death pathway initiated via p20Bap31. *Biochimica et Biophysica Acta-Molecular Cell Research*, *1823*(2), 335–347. https://doi.org/10.1016/j.bbamcr.2011.11.020

Hedskog, L., Pinho, C. M., Filadi, R., Ronnback, A., Hertwig, L., Wiehager, B., Larssen, P., Gellhaar, S., Sandebring, A., Westerlund, M., Graff, C., Winblad, B., Galter, D., Behbahani, H., Pizzo, P., Glaser, E., & Ankarcrona, M. (2013). Modulation of the endoplasmic reticulum-mitochondria interface in Alzheimer's disease and related models. *Proceedings of the National Academy of Sciences of the United States of America*, *110*(19), 7916–7921. https://doi.org/10.1073/pnas.1300677110

Hendrickx, N., Volanti, C., Moens, U., Seternes, O. M., de Witte, P., Vandenheede, J. R., Piette, J., & Agostinis, P. (2003). Up-regulation of cyclooxygenase-2 and apoptosis resistance by p38 MAPK in hypericin-mediated photodynamic therapy of human cancer cells. *Journal of Biological Chemistry*, *278*(52), 52231–52239. https://doi.org/10.1074/jbc.M307591200

Hirota, Y., & Tanaka, Y. (2009). A small GTPase, human Rab32, is required for the formation of autophagic vacuoles under basal conditions. *Cellular and Molecular Life Sciences*, *66*(17), 2913–2932. https://doi.org/10.1007/s00018-009-0080-9

Huang, Y., Bai, Y., Zhao, L., Hu, T., Hu, B. R., Wang, J. L., & Xiang, J. Z. (2007). Pharmacokinetics and metabolism of neferine in rats after a single oral administration. *Biopharmaceutics & Drug Disposition*, *28*(7), 361–372. https://doi.org/10.1002/bdd.556

Iwasawa, R., Mahul-Mellier, A.-L., Datler, C., Pazarentzos, E., & Grimm, S. (2011). Fis1 and Bap31 bridge the mitochondria-ER interface to establish a platform for apoptosis induction. *EMBO Journal*, *30*(3), 556–568. https://doi.org/10.1038/emboj.2010.346

Kim, K. M., Adachi, T., Nielsen, P. J., Terashima, M., Lamers, M. C., Kohler, G., & Reth, M. (1994). 2 new proteins preferentially associated with membrane immunoglobulin-D. *EMBO Journal*, *13*(16), 3793–3800. https://doi.org/10.1002/j.1460-2075.1994.tb06690.x

Korobova, F., Ramabhadran, V., & Higgs, H. N. (2013). An actin-dependent step in mitochondrial fission mediated by the ER-associated formin INF2. *Science*, *339*(6118), 464–467. https://doi.org/10.1126/science.1228360

Kuijpers, M., van Dis, V., Haasdijk, E. D., Harterink, M., Vocking, K., Post, J. A., Scheper, W., Hoogenraad, C. C., & Jaarsma, D. (2013). Amyotrophic lateral sclerosis (ALS)-associated VAPB-P56S inclusions represent an ER quality control compartment. *Acta Neuropathologica Communications*, *1*, 24. https://doi.org/10.1186/2051-5960-1-24

Lakhan, S. E., Kirchgessner, A., & Hofer, M. (2009). Inflammatory mechanisms in ischemic stroke: Therapeutic approaches. *Journal of Translational Medicine*, *7*, 97. https://doi.org/10.1186/1479-5876-7-97

Li, G., Jiang, X., Liang, X., Hou, Y., Zang, J., Zhu, B., Jia, C., Niu, K., Liu, X., Xu, X., Jiang, R., & Wang, B. (2023). BAP31 regulates the expression of ICAM-1/VCAM-1 via MyD88/NF-KB pathway in acute lung injury mice model. *Life Sciences*, *313*, 121310. https://doi.org/10.1016/j.lfs.2022.121310

Lilley, E., Stanford, S. C., Kendall, D. E., Alexander, S. P. H., Cirino, G., Docherty, J. R., George, C. H., Insel, P. A., Izzo, A. A., Ji, Y., Panettieri, R. A., & Ahluwalia, A. (2020). ARRIVE 2.0 and the British Journal of Pharmacology: Updated guidance for 2020. *British Journal of Pharmacology*, *177*(16), 3611–3616. https://doi.org/10.1111/bph.15178

Liu, X., Jiao, K., Jia, C.-c., Li, G.-x., Yuan, Q., Xu, J.-k., Hou, Y., & Wang, B. (2019). BAP31 regulates IRAK1-dependent neuroinflammation in microglia. *Journal of Neuroinflammation*, *16*(1), 281. https://doi.org/10.1186/s12974-019-1661-7

Liu, X., Yuan, Q., Li, G. X., Jia, C. C., Liu, J. Y., Yang, Y. Q., Wang, X. Y., Hou, Y., & Wang, B. (2021). Regulation of superoxide by bap31 through its effect on $p22^{phox}$ and Keap1/Nrf2/HO-1 signaling pathway in microglia. *Oxidative Medicine and Cellular Longevity*, *2021*, 1457089. https://doi.org/10.1155/2021/1457089

Marchi, S., Patergnani, S., & Pinton, P. (2014). The endoplasmic reticulum-mitochondria connection: One touch, multiple functions. *Biochimica et Biophysica Acta-Bioenergetics*, *1837*(4), 461–469. https://doi.org/10.1016/j.bbabio.2013.10.015

Myhill, N., Lynes, E. M., Nanji, J. A., Blagoveshchenskaya, A. D., Fei, H., Simmen, K. C., Cooper, T. J., Thomas, G., & Simmen, T. (2008). The subcellular distribution of calnexin is mediated by PACS-2. *Molecular*

Biology of the Cell, *19*(7), 2777–2788. https://doi.org/10.1091/mbc.E07-10-0995

Namba, T. (2019). BAP31 regulates mitochondrial function via interaction with Tom40 within ER-mitochondria contact sites. *Science Advances*, *5*(6), eaaw1386. https://doi.org/10.1126/sciadv.aaw1386

Namba, T., Tian, F., Chu, K., Hwang, S.-Y., Yoon, K. W., Byun, S., Hiraki, M., Mandinova, A., & Lee, S. W. (2013). CDIP1-BAP31 complex transduces apoptotic signals from endoplasmic reticulum to mitochondria under endoplasmic reticulum stress. *Cell Reports*, *5*(2), 331–339. https://doi.org/10.1016/j.celrep.2013.09.020

Ng, F. W. H., Nguyen, M., Kwan, T., Branton, P. E., Nicholson, D. W., Cromlish, J. A., & Shore, G. C. (1997). p28 Bap31, a Bcl-2/Bcl-X-L- and procaspase-8-associated protein in the endoplasmic reticulum. *Journal of Cell Biology*, *139*(2), 327–338. https://doi.org/10.1083/jcb.139.2.327

Nguyen, M., Breckenridge, D. G., Ducret, A., & Shore, G. C. (2000). Caspase-resistant BAP31 inhibits Fas-mediated apoptotic membrane fragmentation and release of cytochrome c from mitochondria. *Molecular and Cellular Biology*, *20*(18), 6731–6740. https://doi.org/10.1128/mcb.20.18.6731-6740.2000

Niu, K., Xu, J., Cao, Y., Hou, Y., Shan, M., Wang, Y., Xu, Y., Sun, M., & Wang, B. (2017). BAP31 is involved in T cell activation through TCR signal pathways. *Scientific Reports*, *7*, 44809. https://doi.org/10.1038/srep44809

Panaretakis, T., Kepp, O., Brockmeier, U., Tesniere, A., Bjorklund, A.-C., Chapman, D. C., Durchschlag, M., Joza, N., Pierron, G., Van Endert, P., Yuan, J., & Kroemer, G. (2009). Mechanisms of pre-apoptotic calreticulin exposure in immunogenic cell death. *EMBO Journal*, *28*(5), 578–590. https://doi.org/10.1038/emboj.2009.1

Quistgaard, E. M., Low, C., Moberg, P., Guettou, F., Maddi, K., & Nordlund, P. (2013). Structural and biophysical characterization of the cytoplasmic domains of human BAP29 and BAP31. *PLoS ONE*, *8*(8), e71111. https://doi.org/10.1371/journal.pone.0071111

Radford, S. E. (2006). GroEL: More than just a folding cage. *Cell*, *125*(5), 831–833. https://doi.org/10.1016/j.cell.2006.05.021

Rao, J., Yue, S., Fu, Y., Zhu, J., Wang, X., Busuttil, R. W., Kupiec-Weglinski, J. W., Lu, L., & Zhai, Y. (2014). ATF6 mediates a pro-inflammatory synergy between ER stress and TLR activation in the pathogenesis of liver ischemia-reperfusion injury. *American Journal of Transplantation*, *14*(7), 1552–1561. https://doi.org/10.1111/ajt.12711

Rimessi, A., Marchi, S., Fotino, C., Romagnoli, A., Huebner, K., Croce, C. M., Pinton, P., & Rizzuto, R. (2009). Intramitochondrial calcium regulation by the FHIT gene product sensitizes to apoptosis. *Proceedings of the National Academy of Sciences of the United States of America*, *106*(31), 12753–12758. https://doi.org/10.1073/pnas.0906484106

Rizzuto, R., Brini, M., Murgia, M., & Pozzan, T. (1993). Microdomains with high Ca^{2+} close to ip(3)-sensitive channels that are sensed by neighboring mitochondria. *Science*, *262*(5134), 744–747. https://doi.org/10.1126/science.8235595

Szabadkai, G., Bianchi, K., Varnai, P., De Stefani, D., Wieckowski, M. R., Cavagna, D., Nagy, A. I., Balla, T., & Rizzuto, R. (2006). Chaperone-mediated coupling of endoplasmic reticulum and mitochondrial Ca^{2+} channels. *Journal of Cell Biology*, *175*(6), 901–911. https://doi.org/10.1083/jcb.200608073

Wang, T., Chen, J., Hou, Y., Yu, Y., & Wang, B. (2019). BAP31 deficiency contributes to the formation of amyloid-β plaques in Alzheimer's disease by reducing the stability of RTN3. *FASEB Journal*, *33*(4), 4936–4946. https://doi.org/10.1096/fj.201801702R

Yamazaki, H., Hiramatsu, N., Hayakawa, K., Tagawa, Y., Okamura, M., Ogata, R., Huang, T., Nakajima, S., Yao, J., Paton, A. W., Paton, J. C., & Kitamura, M. (2009). Activation of the Akt-NF-κB pathway by subtilase cytotoxin through the ATF6 branch of the unfolded protein response. *Journal of Immunology*, *183*(2), 1480–1487. https://doi.org/10.4049/jimmunol.0900017

Yang, L., Zhou, R. Y., Tong, Y., Chen, P. F., Shen, Y., Miao, S., & Liu, X. Q. (2020). Neuroprotection by dihydrotestosterone in LPS-induced neuroinflammation. *Neurobiology of Disease*, *140*, 104814. https://doi.org/10.1016/j.nbd.2020.104814

Zen, K., Utech, M., Liu, Y., Soto, I., Nusrat, A., & Parkos, C. A. (2004). Association of BAP31 with CD11b/CD18 - potential role in intracellular trafficking of CD11b/CD18 in neutrophils. *Journal of Biological Chemistry*, *279*(43), 44924–44930. https://doi.org/10.1074/jbc.M402115200

Zhao, B., An, F., Hao, Z., Zhang, W., & Wang, B. (2024). BAP31 plays an essential role in mouse B cell development via regulation of BCR signaling. *International Journal of Molecular Sciences*, *25*(9), 4962. https://doi.org/10.3390/ijms25094962

Zhao, L., Wang, X., Chang, Q., Xu, J., Huang, Y., Guo, Q., Zhang, S., Wang, W., Chen, X., & Wang, J. (2010). Neferine, a bisbenzylisoquinline alkaloid attenuates bleomycin-induced pulmonary fibrosis. *European Journal of Pharmacology*, *627*(1–3), 304–312. https://doi.org/10.1016/j.ejphar.2009.11.07

Zhao, Y., Hellum, B. H., Liang, A., & Nilsen, O. G. (2012). The in vitro inhibition of human CYP1A2, CYP2D6 and CYP3A4 by tetrahydropalmatine, neferine and berberine. *Phytotherapy Research*, *26*(2), 277–283. https://doi.org/10.1002/ptr.3554

SUPPORTING INFORMATION

Additional supporting information can be found online in the Supporting Information section at the end of this article.

How to cite this article: Zhu, Y.-X., Yang, Z., Li, L., Chen, Z.-K., Zhuo, F.-F., Wang, Y.-H., Liu, Z.-P., Han, B., Yu, W., Tu, P.-F., Wei, T.-T., Wang, H., & Zeng, K.-W. (2025). Molecular glue neferine induces BAP31 homodimerisation to disrupt endoplasmic reticulum–mitochondria crosstalk for anti-neuroinflammation in ischaemic stroke. *British Journal of Pharmacology*, 1–23. https://doi.org/10.1111/bph.70277